

# SALT spectroscopic observations of galaxy clusters detected by ACT and a Type II quasar hosted by a brightest cluster galaxy

Brian Kirk,<sup>1,2\*</sup> Matt Hilton,<sup>1,3†</sup> Catherine Cress,<sup>2,4</sup> Steven M. Crawford,<sup>5</sup> John P. Hughes,<sup>6</sup> Nicholas Battaglia,<sup>7</sup> J. Richard Bond,<sup>8</sup> Claire Burke,<sup>1</sup> Megan B. Gralla,<sup>9</sup> Amir Hajian,<sup>8</sup> Matthew Hasselfield,<sup>10</sup> Adam D. Hincks,<sup>11</sup> Leopoldo Infante,<sup>12</sup> Arthur Kosowsky,<sup>13</sup> Tobias A. Marriage,<sup>9</sup> Felipe Menanteau,<sup>14</sup> Kavilan Moodley,<sup>1</sup> Michael D. Niemack,<sup>15</sup> Jonathan L. Sievers,<sup>16</sup> Cristóbal Sifón,<sup>17</sup> Susan Wilson,<sup>1</sup> Edward J. Wollack,<sup>18</sup> and Caroline Zunckel<sup>16</sup>

<sup>1</sup> Astrophysics & Cosmology Research Unit, School of Mathematics, Statistics & Computer Science, University of KwaZulu-Natal, Durban 4041, SA

<sup>2</sup> Centre for High Performance Computing, CSIR Campus, 15 Lower Hope St. Rosebank, Cape Town, SA

<sup>3</sup> Centre for Astronomy & Particle Theory, School of Physics and Astronomy, University of Nottingham, NG7 2RD, UK

<sup>4</sup> Department of Physics, University of Western Cape, Bellville 7530, Cape Town, SA

<sup>5</sup> South African Astronomical Observatory, P.O. Box 9, Observatory 7935, Cape Town, SA

<sup>6</sup> Department of Physics and Astronomy, Rutgers, The State University of New Jersey, 136 Frelinghuysen Road, Piscataway, NJ USA 08854-8019

<sup>7</sup> McWilliams Center for Cosmology, Carnegie Mellon University, Department of Physics, 5000 Forbes Ave., Pittsburgh PA, USA, 15213

<sup>8</sup> Canadian Institute for Theoretical Astrophysics, 60 St George, Toronto ON, Canada, M5S 3H8

<sup>9</sup> Department of Physics and Astronomy, Johns Hopkins University, 3400 N. Charles St., Baltimore, MD 21218

<sup>10</sup> Department of Astrophysical Sciences, Peyton Hall, Princeton University, Princeton, NJ 08544, USA

<sup>11</sup> Department of Physics and Astronomy, University of British Columbia, 6224 Agricultural Road, Vancouver, BC V6T 1Z1, Canada

<sup>12</sup> Departamento de Astronomía y Astrofísica, Pontificia Universidad Católica, Casilla 306, Santiago 22, Chile

<sup>13</sup> Department of Physics and Astronomy, University of Pittsburgh, Pittsburgh, PA 15260 USA

<sup>14</sup> National Center for Supercomputing Applications, University of Illinois at Urbana-Champaign, 1205 W. Clark St, Urbana, IL 61801

<sup>15</sup> Department of Physics, Cornell University, Ithaca, NY 14853, USA

<sup>16</sup> Astrophysics & Cosmology Research Unit, School of Chemistry & Physics, University of KwaZulu-Natal, Durban 4041, SA

<sup>17</sup> Leiden Observatory, Leiden University, PO Box 9513, NL-2300 RA Leiden, Netherlands

<sup>18</sup> NASA/Goddard Space Flight Center, Greenbelt, MD, 20771, USA

Accepted for publication in MNRAS

## ABSTRACT

We present Southern African Large Telescope (SALT) follow-up observations of seven massive clusters detected by the Atacama Cosmology Telescope (ACT) on the celestial equator using the Sunyaev-Zel’dovich (SZ) effect. We conducted multi-object spectroscopic observations with the Robert Stobie Spectrograph in order to measure galaxy redshifts in each cluster field, determine the cluster line-of-sight velocity dispersions, and infer the cluster dynamical masses. We find that the clusters, which span the redshift range  $0.3 < z < 0.55$ , range in mass from  $(5 - 20) \times 10^{14} M_{\odot}$  ( $M_{200c}$ ). Their masses, given their SZ signals, are similar to those of southern hemisphere ACT clusters previously observed using Gemini and the VLT. We note that the brightest cluster galaxy in one of the systems studied, ACT-CL J0320.4+0032 at  $z = 0.38$ , hosts a Type II quasar. Only a handful of such systems are currently known, and therefore ACT-CL J0320.4+0032 may be a rare example of a very massive halo in which quasar-mode feedback is actively taking place.

**Key words:** cosmology: observations – galaxies: clusters: general – galaxies: clusters: individual: ACT-CL J0320.4+0032 – galaxies: quasars: general

## 1 INTRODUCTION

Clusters of galaxies mark the highest density regions of the Universe at mega parsec scales. By charting the evolution of their num-

\* E-mail: bmarshallk@gmail.com

† E-mail: hiltonm@ukzn.ac.za

ber density as a function of mass and redshift, one is able to obtain constraints on cosmological parameters, including the amount of dark matter and dark energy in the Universe (e.g., Vikhlinin et al. 2009; Mantz et al. 2010; Sehgal et al. 2011; Benson et al. 2013; Hasselfield et al. 2013; Planck Collaboration 2013). However, cluster mass – which is the property predicted by  $N$ -body simulations of cold dark matter – is not a directly measurable quantity, and must instead be inferred from the observable properties of the clusters. This has led to many studies that derive mass–observable scaling relations using a wide variety of observables including, optical richness (e.g., Rozo et al. 2009); X-ray luminosity and temperature (e.g., Vikhlinin et al. 2006); and Sunyaev-Zel’dovich effect signal (e.g., Sifón et al. 2013).

The discovery of new clusters from large area surveys using the Sunyaev-Zel’dovich effect (SZ; Sunyaev & Zel’dovich 1970) began only in recent years (e.g., Staniszewski et al. 2009; Vanderlinde et al. 2010; Marriage et al. 2011; Reichardt et al. 2013; Planck Collaboration et al. 2013; Bleem et al. 2014). The SZ effect is the inverse Compton scattering of cosmic microwave background photons by hot ( $> 10^7$  K) gas trapped within the deep gravitational potential wells of massive galaxy clusters. It is almost redshift independent, and in principle, it allows the discovery of all clusters in the Universe above a mass limit set by the noise properties of the SZ survey (see, e.g., Birkinshaw 1999; Carlstrom et al. 2002). In addition, the SZ signal, usually denoted by the integrated Comptonisation ( $Y$ ) parameter, has been shown to correlate with cluster mass, with relatively small scatter (e.g., Planck Collaboration et al. 2011; Hoekstra et al. 2012; Sifón et al. 2013). Despite this, mass–calibration is the main contribution to the error budget of current cosmological studies using SZ-selected cluster samples (e.g., Sehgal et al. 2011; Hasselfield et al. 2013; Reichardt et al. 2013; Planck Collaboration 2013; Bocquet et al. 2014), and so further work in this area is clearly needed.

In this paper, we present the results of a pilot follow-up study of SZ-selected clusters detected by the Atacama Cosmology Telescope (ACT; Swetz et al. 2011) conducted using the Robert Stobie Spectrograph (RSS; Burgh et al. 2003) on the Southern African Large Telescope (SALT; Buckley et al. 2006). The goals of this programme were to obtain spectroscopic redshifts and dynamical mass estimates through velocity dispersions for ACT clusters, with the aim of increasing the sample of clusters for our calibration of the  $Y$ -mass relation (Sifón et al. 2013; see Hasselfield et al. 2013 for joint constraints on the dynamical mass scaling relation and cosmological parameters).

The structure of this paper is as follows. We briefly describe the ACT cluster sample and the design, execution, and reduction of the SALT spectroscopic observations in Section 2. Section 3 presents the cluster redshifts and velocity dispersions. We compare the properties of the clusters studied here to previous observations of SZ clusters in Section 4 and summarise our findings in Section 5.

We assume a cosmology with  $\Omega_m = 0.3$ ,  $\Omega_\Lambda = 0.7$ , and  $H_0 = 70 \text{ km s}^{-1} \text{ Mpc}^{-1}$  throughout. All magnitudes are on the AB system (Oke 1974), unless otherwise stated.

## 2 OBSERVATIONS AND ANALYSIS

### 2.1 Cluster sample

The clusters targeted for SALT observations were drawn from the SZ-selected sample constructed by the ACT team (Hasselfield et al. 2013; Menanteau et al. 2013). ACT (Swetz et al. 2011) is a 6 m tele-

scope located in northern Chile that observes the sky in three frequency bands (centred at 148, 218, and 277 GHz) simultaneously with arcminute resolution.

ACT surveyed two regions of the sky, searching a total area of  $959 \text{ deg}^2$  for SZ galaxy clusters. During 2008, ACT observed a  $455 \text{ deg}^2$  patch of the Southern sky, centred on  $\delta = -55 \text{ deg}$ , detecting a total of 23 massive clusters that were optically confirmed using 4 m class telescopes (Menanteau et al. 2010; Marriage et al. 2011). From 2009–2010, ACT observed a  $504 \text{ deg}^2$  region centred on the celestial equator, an area chosen due to its complete overlap with the deep ( $r \approx 23.5 \text{ mag}$ ) optical data from the  $270 \text{ deg}^2$  Stripe 82 region (Annis et al. 2011) of the Sloan Digital Sky Survey (SDSS; Abazajian et al. 2009). Hasselfield et al. (2013) describes the construction of the SZ cluster sample from the 148 GHz maps (see Dünner et al. 2013 for a detailed description of the reduction of the ACT data from timestreams to maps). Optical confirmation and redshifts for these clusters are reported in Menanteau et al. (2013), using data from SDSS and additional targeted optical and IR observations obtained at Apache Point Observatory. All 68 clusters in the sample have either photometric redshift estimates, or spectroscopic redshifts (largely derived from SDSS data). The sample spans the redshift range  $0.1 < z < 1.4$ , with median  $z = 0.5$ .

In this pilot study with SALT, we targeted seven of the equatorial ACT clusters detected with reasonably high signal-to-noise ( $4.6 < S/N < 8.3$ ) and at moderate redshift ( $z \approx 0.4$ ), in order to ensure that targeted galaxies would be bright enough for successful absorption line redshift measurements given the capabilities of the RSS instrument at the time of the observations<sup>1</sup>. Sifón et al. (in prep.) will present observations of a further 21 ACT equatorial clusters observed with the Gemini telescopes.

### 2.2 Spectroscopic observations

We conducted observations of the seven target ACT clusters with RSS in multi-object spectroscopy (MOS) mode, which uses custom designed slit masks. Given that SALT is located at Sutherland where the median seeing is  $1.3''$  (Catala et al. 2013), we chose to use slitlets with dimensions of  $1.5''$  width and  $10''$  length. The latter was chosen to ensure reasonably accurate sky subtraction given these seeing conditions. The RSS has an  $8'$  diameter circular field of view, and with these slit dimensions we found we were able to target 19–26 galaxies in each cluster field per slit mask. We selected 3–4 bright ( $15 - 17.5$  magnitude in the  $r$  band) stars per cluster field for alignment of the slit masks during acquisition.

The slit masks were designed using catalogues extracted from the 8th data release of the SDSS (SDSS; Aihara et al. 2011). We centred each slit mask on the Brightest Cluster Galaxy (BCG) coordinates listed in Menanteau et al. (2013) and estimated the colour of the red-sequence from visual inspection of the colour-magnitude diagrams. We used this information to define target galaxy samples for each cluster, prioritising the selection of galaxies with magnitudes fainter than the BCG and with colour bluer than our estimate of the red-edge of the red-sequence (note that these colour - magnitude cuts vary from cluster-to-cluster due to their slightly different redshifts). We then proceeded to assign slits to target galaxies in an automated fashion using an algorithm that prioritised objects closer to the cluster centre (in practice, this ensured that the number of objects whose spectra were centred horizontally on the detector

<sup>1</sup> At the time of writing (September 2014), RSS is undergoing refurbishment that aims to increase its throughput considerably.

**Table 1.** Details of spectroscopic observations reported in this work. For all observations the pg0900 grating was used with the pc03850 order blocking filter. The CS and GA columns indicate the RSS camera station and grating angle used respectively. Slitlets in all masks were  $1.5''$  wide and  $10''$  long. The position angle for all observations was  $180^\circ$ , as all targets are on the celestial equator. The number of slits ( $N_{\text{slits}}$ ) does not include alignment stars. Time allocations by SALT partner: RSA 50 per cent, Rutgers 50 per cent.

Program	Target	Mask	$N_{\text{slits}}$	Frames (sec)	CS (deg)	GA (deg)	Airmass	Seeing (arcsec)	Date(s) (UT)
2012-1-RSA_UKSC_RU-001	J2058.8+0123	1	23	$2 \times 975$	28.75	14.375	1.8	1.6	2012 Jul 16
2012-1-RSA_UKSC_RU-001	J2058.8+0123	2	22	$2 \times 975$	28.75	14.375	1.3	1.5	2012 Jul 24
2012-1-RSA_UKSC_RU-001	J2058.8+0123	3	22	$2 \times 975$	28.75	14.375	1.3	1.4	2012 Sep 06
2012-2-RSA_UKSC_RU-001	J0320.4+0032	1	25	$2 \times 975$	28.75	14.375	1.3	1.3	2012 Nov 10
2012-2-RSA_UKSC_RU-001	J0320.4+0032	2	26	$4 \times 975$	28.75	14.375	1.3,1.3	0.9,1.4	2012 Nov 13, 15
2012-2-RSA_UKSC_RU-001	J0320.4+0032	3	22	$4 \times 975$	28.75	14.375	1.3	1.3	2012 Nov 16
2012-2-RSA_UKSC_RU-001	J0219.9+0129	1	22	$4 \times 975$	28.75	14.375	1.3,1.3	1.4, 1.3	2012 Nov 15, 16
2013-1-RSA_RU-001	J0045.2-0152	1	26	$4 \times 975$	32.50	16.250	1.2,1.2	1.2,1.4	2013 Sep 01, 05
2013-1-RSA_RU-001	J0045.2-0152	2	25	$2 \times 975$	32.50	16.250	1.2	1.5	2013 Sep 25
2013-2-RSA_RU-002	J0156.4-0123	1	25	$2 \times 975$	31.00	15.50	1.2	1.6	2013 Nov 02
2013-2-RSA_RU-002	J0156.4-0123	3	21	$2 \times 975$	31.00	15.50	1.3	1.3	2014 Jan 03
2013-2-RSA_RU-002	J0348.6-0028	1	25	$2 \times 975$	28.75	14.375	1.2	1.4	2013 Nov 03
2013-2-RSA_RU-002	J0348.6-0028	2	23	$2 \times 975$	28.75	14.375	2.0	1.9	2014 Jan 01
2013-2-RSA_RU-002	J0348.6-0028	3	23	$4 \times 975$	28.75	14.375	1.3,1.2	1.5, 0.8	2013 Nov 04, 08
2013-2-RSA_RU-002	J0348.6-0028	4	19	$4 \times 975$	28.75	14.375	1.3,1.3	1.4,1.5	2013 Dec 29, 30
2013-2-RSA_RU-002	J0342.7-0017	1	22	$2 \times 975$	28.00	14.000	1.2	1.3	2014 Jan 03

array was maximised). The final masks were made using the PYS-LITMASK tool, part of the PYSALT<sup>2</sup> software package (Crawford et al. 2010). We designed multiple masks for each target, although not all masks were observed.

The RSS observations were conducted using the pg0900 Volume Phase Holographic (VPH) grating. We set the RSS camera station and grating angle to centre the wavelength coverage at the expected wavelength of D4000 for each cluster, since each cluster had either a spectroscopic or photometric redshift measurement (Menanteau et al. 2013). The observing set up for  $z \approx 0.3$  clusters (i.e., most clusters in this sample; camera station  $28.75^\circ$ , grating angle  $14.375^\circ$ ) results in dispersion  $0.98 \text{ \AA}$  per binned pixel ( $2 \times 2$  binning) with  $4000 - 7000 \text{ \AA}$  wavelength coverage. This results in a resolution of  $\sim 4 \text{ \AA}$ . There are two gaps in the spectral coverage due to physical gaps between three CCD chips that read out the dispersed spectra.

The design of SALT limits observations of objects on the celestial equator to approximately 3200 sec long intervals (referred to as observing blocks or tracks). In each observing block the position of the tracker must be reset and the object re-acquired, the mask must be aligned, and flats and arcs must be obtained. These operations incur significant overhead ( $\approx 1200$  sec in total per block). We therefore obtained  $2 \times 975$  sec RSS exposures per observing block for our first observations in July-September 2012. For some subsequent observations, we obtained  $4 \times 975$  sec exposures by observing each mask in two observing blocks. Note that SALT is a queue-scheduled telescope and observations were obtained (sometimes of the same mask) on different nights throughout each observing semester. Table 1 presents a summary of the observations.

### 2.3 Spectroscopic data reduction

A combination of PYSALT and IRAF<sup>3</sup> tasks were used to reduce the spectra. PYSALT is a suite of PYRAF tools for the reduction

and analysis of data obtained from the RSS instrument mounted on SALT (see Crawford et al. 2010). PYSALT tasks were used to prepare the image headers for the pipeline; apply CCD amplifier gain and crosstalk corrections; subtract bias frames; perform cleaning of cosmic-rays; apply flat-field corrections; create mosaic images; and extract the data for each target based on the slit mask geometry. IRAF tasks were then used to determine a wavelength dispersion function from a calibration lamp (Xenon or Argon); fit and transform the arc dispersion to the science frames; apply a background subtraction to each slitlet, the value of which is determined by a constant sampling area across the dispersion axis; combine images; and extract one dimensional spectra. For combined images, a maximum wavelength shift of  $0.2 \text{ \AA}$  was measured between nights for observations of the same objects, well within the spectrograph resolution.

### 2.4 Galaxy redshift measurements

Galaxy redshifts were measured by cross-correlating the spectra with SDSS galaxy spectral templates<sup>4</sup> using the RVSAO/XCSAO package for IRAF (Kurtz & Mink 1998). We ran the cross-correlation repeatedly with starting redshifts spanning  $0.0 < z < 1$  in intervals of  $\delta z = 0.0001$  for six different templates. We selected the redshift with the highest correlation coefficient as the best measurement for the given template. This method provided six possible redshifts per galaxy spectrum. The final redshift measurement for each galaxy was selected from these six candidate redshifts after visual inspection of the 1d and 2d spectra by two or more of the co-authors.

<sup>2</sup> The PySALT user package is the primary reduction and analysis software tools for the SALT telescope (<http://pysalt.salt.ac.za/>).

<sup>3</sup> IRAF is distributed by the National Optical Astronomy Observatories, which are operated by the Association of Universities for Research in Astronomy, Inc., under cooperative agreement with the National Science Foundation.

<sup>4</sup> <http://www.sdss.org/dr7/algorithms/spectemplates/index.html>

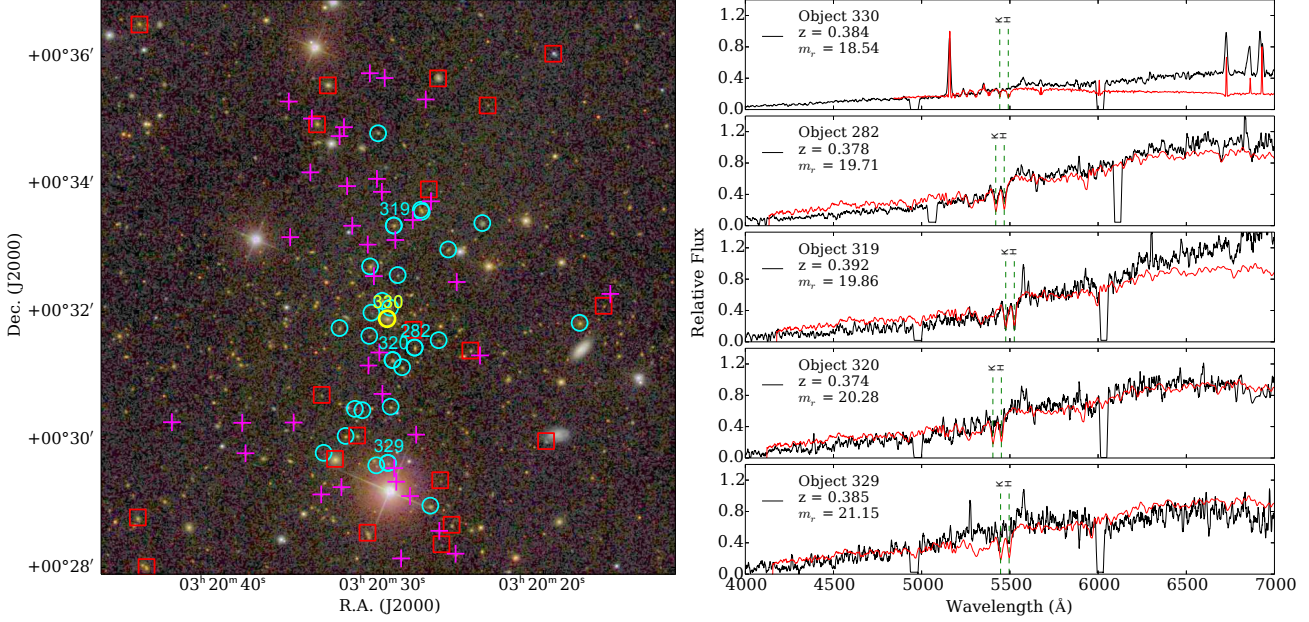


**Figure 1.** The  $z = 0.38$  cluster ACT-CL J0320.4+0032. The left hand panel shows a  $9' \times 9'$  false colour SDSS optical image ( $g, r, i$ ). Objects highlighted with cyan circles are spectroscopically confirmed members (see Section 3.2; spectra for objects marked with ID numbers are shown in the right hand panel); red squares mark non-members with confirmed redshifts; and magenta crosses mark objects for which we failed to measure a secure redshift ( $Q < 3$ ; see Section 2.4). In the right hand panel, black lines correspond to SALT RSS spectra (smoothed with a 10 pixel boxcar), while red lines show the best match redshifted SDSS spectral template in each case. The displayed object spectra span a representative range in  $r$ -band magnitudes, as indicated in the figure, and the spectrum for the brightest object is that of the BCG. In this case, the BCG (object 330) is a Type II quasar (see Section 4.2; it is highlighted with the yellow circle in the image). Similar figures for the other clusters can be found in the Appendix.

We defined a quality rating system ( $Q$ ) to describe the confidence level of each redshift measurement (e.g., Wirth et al. 2004). Galaxies exhibiting multiple absorption and/or emission features were given a  $Q = 4$  rating;  $Q = 3$  corresponds to galaxies exhibiting a single, strongly detected feature; galaxies showing the proper  $z$  range but exhibiting no strong features were  $Q = 2$ ; and galaxies with clearly spurious  $z$  values (where the cross correlation failed due to poor signal-to-noise) and no strong features were rated  $Q = 1$ . Redshift measurements with  $Q < 3$  were as a result of poor signal-to-noise spectra, slits blocked by the guide probe, or telescope malfunctions such as slit mask alignment failure resulting in manual alignment.

Spectra of members of each cluster, overplotted with best match spectral templates at the measured redshifts, are presented in Fig. 1 (for ACT-CL J0320.4+0032) and Figs. A1–A6 in the Appendix for the other clusters in the sample. In these figures, the left hand panel shows a  $9' \times 9'$  false colour SDSS optical image ( $g, r, i$ ) of the cluster, highlighting galaxies for which redshifts were measured. In the right hand panel, a selection of spectra spanning the magnitude range of the members are shown, and the spectrum for the brightest object is that of the BCG. In the case of ACT-CL J0320.4+0032, we see relatively broad emission lines in the spectrum of the BCG (Fig. 1). As discussed in Section 4, this galaxy is a Type II quasar host, and this may be a rare example of a massive cluster in which quasar-mode feedback is observed to be actively taking place.

Since all of our clusters are located within the SDSS footprint, we were able to verify the SALT redshift measurements using a small number of objects in common with SDSS DR10 (Ahn et al. 2014). From 9 overlapping galaxies, we found that the median  $\delta z = z_{\text{SALT}} - z_{\text{SDSS}} = -1.0 \times 10^{-5}$ , with standard deviation

$\sigma = 3.9 \times 10^{-4}$  (we take the latter to indicate the level of uncertainty in the SALT redshift measurements). At  $z = 0.3$ , these translate into a median rest-frame velocity offset of  $-2.3 \text{ km s}^{-1}$  with  $\sigma = 90 \text{ km s}^{-1}$ . Given the relatively low redshift of the clusters in this study, a search of SDSS DR10 also yielded some additional spectroscopic redshifts within most of the clusters that were not matched with galaxies targeted by SALT. These objects are included in the analysis presented in Section 3 below.

## 2.5 Redshift success rate

Since this project is one of the first to use the MOS mode of RSS to collect galaxy redshifts, here we quantify our efficiency for the benefit of others planning to use this instrument for similar work. Fig. 2 shows the redshift measurement success rate as a function of galaxy  $r$ -band magnitude, where we define a successful redshift measurement as one with  $Q \geq 3$  (note that only galaxies with  $Q \geq 3$  are included in the sample used to measure cluster velocity dispersions, as described in Section 3 below). Overall, we successfully measured redshifts for 191 out of 372 galaxies targeted (51 per cent), spanning the  $r$ -band magnitude range 17.9–23.9; the top panels in Fig. 2 show the magnitude distributions of the target galaxies.

As described in Section 2.2 above, the design of SALT limits observations on the celestial equator to tracks of 3200 sec duration, and we observed some masks with one SALT track per target (obtaining  $2 \times 975$  sec of integration per mask), and others with two SALT tracks per target (obtaining  $4 \times 975$  sec of integration per mask). The columns of Fig. 2 show how the redshift success rate changes depending on whether one or two tracks were used. We see that the two-track observations result in more than double the efficiency for measuring redshifts for galaxies with  $21 < r$ -band mag  $<$

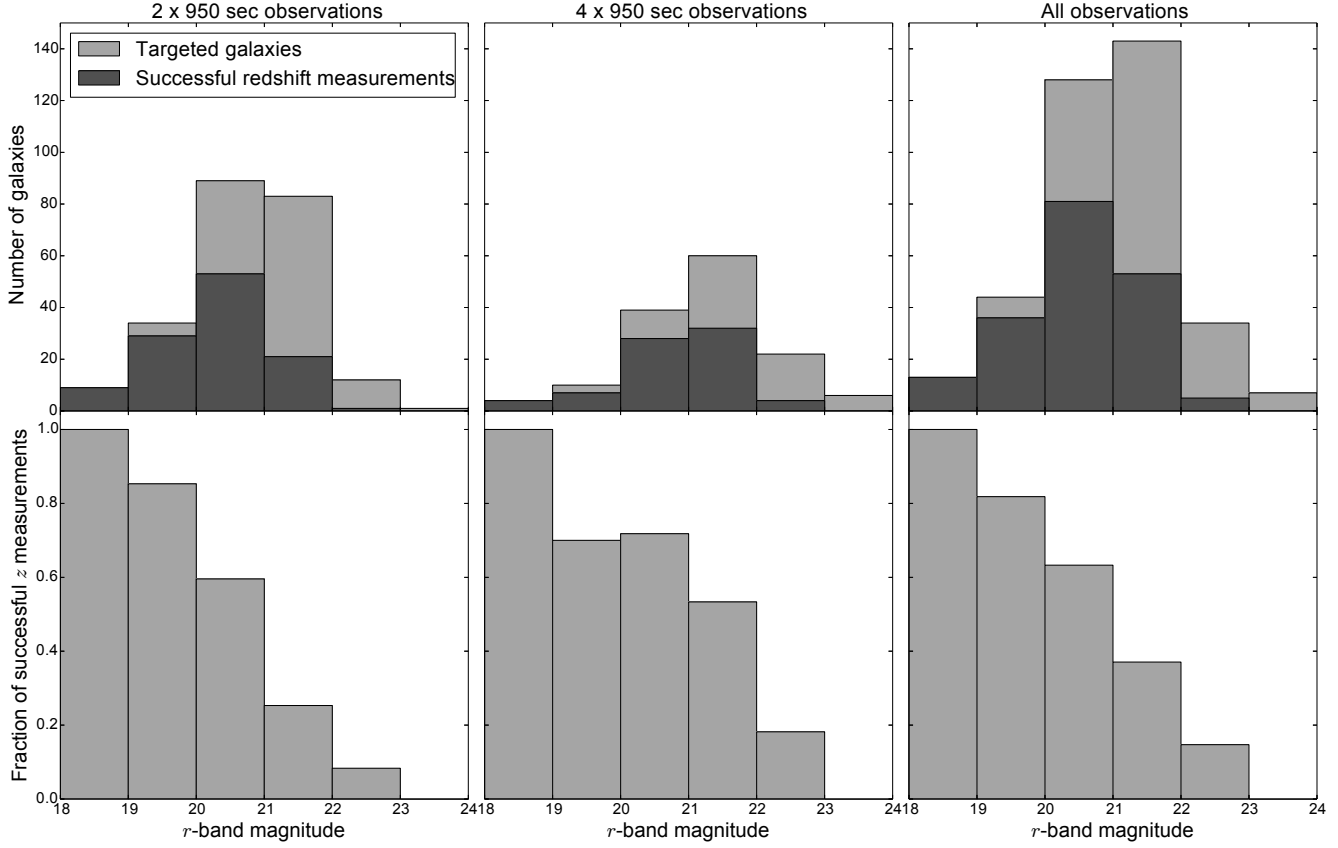


**Figure 2.** Redshift success rate as a function of  $r$ -band magnitude, where a successful redshift measurement is defined as having quality flag  $Q \geq 3$ . Results for  $2 \times 975$  sec of integration (one track),  $4 \times 975$  sec of integration (two tracks), and all observations are shown in the columns. Note that no attempt is made to control for the effect of variation in observing conditions.

23. In two-track observations, we successfully measured redshifts for 53 per cent of galaxies with  $21 < r\text{-band mag} < 22$  and 18 per cent of galaxies with  $22 < r\text{-band mag} < 23$ . The magnitude limit corresponding to redshift measurement efficiency of 70 per cent is  $r < 21$  for one track, compared to  $r < 21.4$  for the two track observations. Note that none of the above estimates take into account possible variation in observing conditions between the one versus two track observations, although the seeing was similar (see Table 1).

### 3 RESULTS

In this Section, we describe our measurements of cluster properties: redshift, velocity dispersion, and dynamical mass. Throughout we used only galaxies with secure redshifts ( $Q \geq 3$ ). Where needed, we adopt the coordinates of the BCG (as listed in Menanteau et al. 2013) as the cluster centre.

#### 3.1 Cluster redshift measurements

We used the biweight location (Beers et al. 1990) to estimate cluster redshifts. Firstly, we remove obvious foreground and background galaxies not physically associated with the cluster by applying a  $3000 \text{ km s}^{-1}$  cut relative to the initial cluster redshift (as listed in Menanteau et al. 2013) and removed any galaxies determined to be

interlopers (see Section 3.2 below). We then calculated the biweight location from the remaining galaxies. This procedure was iterated until the estimate for the redshift of the cluster converged. Peculiar velocities for galaxies were then calculated relative to this newly adopted cluster redshift estimate.

#### 3.2 Determining cluster membership

Not all of the galaxies targeted in the SALT RSS field of view are identified as cluster members. For this work, we used an adaptation of the fixed-gap method to identify cluster members. This is similar to the procedure used by Fadda et al. (1996) and further refined in Crawford et al. (2014). We define the peculiar velocity of a galaxy within a cluster as

$$\Delta v_i = c \frac{(z_i - \bar{z})}{(1 + \bar{z})}, \quad (1)$$

where  $\Delta v_i$  is the peculiar velocity of the  $i$ th galaxy,  $z_i$  is its redshift, and  $\bar{z}$  is the redshift of the cluster as estimated using the biweight location (see Section 3.1 above).

To find the interlopers, we sorted all galaxies by their peculiar velocities and identified any adjacent galaxies (in velocity space) with gaps greater than  $1000 \text{ km s}^{-1}$ . De Propris et al. (2002) argue that galaxy clusters correspond to well-defined peaks with respect to recessional velocity and that gaps between successive galaxies of more than  $1000 \text{ km s}^{-1}$  indicate interlopers. We iteratively remove

**Table 2.** Spectroscopic redshifts of galaxies in the direction of ACT-CL J0320.4+0032 measured using SALT RSS:  $m_r$  is the SDSS  $r$ -band magnitude of the object;  $z$  is the redshift;  $Q$  is the redshift quality flag (see Section 2.4); Em. Lines? indicates objects which show emission lines in their spectra (e.g., [OII]  $\lambda$  3727); Member? indicates objects which are determined to be cluster members (see Section 3.2);  $r$  (Mpc) indicates the projected distance from the BCG position as given in Menanteau et al. (2013). Member galaxies in Mask 'S' have redshifts from SDSS DR10 (Ahn et al. 2013). Similar tables for the other clusters are found in the Appendix.

ID	Mask	RA (J2000)	Dec. (J2000)	$m_r$	$z$	$Q$	Em. Lines?	Member?	$r$ (Mpc)
330	1	03 <sup>h</sup> 20 <sup>m</sup> 29 <sup>s</sup> 788	+00°31'53"60	18.54	0.3836	4	✓	✓	0.00
324	2	03 <sup>h</sup> 20 <sup>m</sup> 29 <sup>s</sup> 602	+00°32'03"99	21.73	0.3884	4	...	✓	0.05
356	3	03 <sup>h</sup> 20 <sup>m</sup> 30 <sup>s</sup> 772	+00°31'59"27	21.92	0.3943	4	...	✓	0.09
10	S	03 <sup>h</sup> 20 <sup>m</sup> 30 <sup>s</sup> 096	+00°32'10"41	19.69	0.3883	4	...	✓	0.09
360	1	03 <sup>h</sup> 20 <sup>m</sup> 30 <sup>s</sup> 907	+00°31'37"50	21.75	0.3827	3	...	✓	0.13
286	2	03 <sup>h</sup> 20 <sup>m</sup> 28 <sup>s</sup> 141	+00°31'43"24	22.06	0.4725	3	...	...	...
282	2	03 <sup>h</sup> 20 <sup>m</sup> 28 <sup>s</sup> 066	+00°31'26"50	19.71	0.3778	4	...	✓	0.19
320	2	03 <sup>h</sup> 20 <sup>m</sup> 29 <sup>s</sup> 449	+00°31'14"78	20.28	0.3737	4	...	✓	0.20
311	2	03 <sup>h</sup> 20 <sup>m</sup> 29 <sup>s</sup> 130	+00°32'34"61	21.02	0.3790	4	✓	✓	0.22
396	3	03 <sup>h</sup> 20 <sup>m</sup> 32 <sup>s</sup> 770	+00°31'44"87	20.32	0.3842	4	...	✓	0.24
303	3	03 <sup>h</sup> 20 <sup>m</sup> 28 <sup>s</sup> 853	+00°31'08"07	20.42	0.3867	4	...	✓	0.25
251	3	03 <sup>h</sup> 20 <sup>m</sup> 26 <sup>s</sup> 561	+00°31'33"46	21.44	0.3841	4	✓	✓	0.27
6	S	03 <sup>h</sup> 20 <sup>m</sup> 30 <sup>s</sup> 857	+00°32'42"80	19.46	0.3939	4	...	✓	0.27
323	1	03 <sup>h</sup> 20 <sup>m</sup> 29 <sup>s</sup> 571	+00°30'30"98	20.50	0.3830	4	...	✓	0.43
238	3	03 <sup>h</sup> 20 <sup>m</sup> 25 <sup>s</sup> 962	+00°32'58"63	20.62	0.3791	4	...	✓	0.45
319	1	03 <sup>h</sup> 20 <sup>m</sup> 29 <sup>s</sup> 372	+00°33'21"18	19.86	0.3922	4	...	✓	0.46
368	2	03 <sup>h</sup> 20 <sup>m</sup> 31 <sup>s</sup> 339	+00°30'27"66	21.22	0.3791	3	✓	✓	0.47
376	3	03 <sup>h</sup> 20 <sup>m</sup> 31 <sup>s</sup> 809	+00°30'28"95	20.80	0.3868	4	...	✓	0.47
421	2	03 <sup>h</sup> 20 <sup>m</sup> 33 <sup>s</sup> 887	+00°30'42"03	21.36	0.3293	4	✓	...	...
271	1	03 <sup>h</sup> 20 <sup>m</sup> 27 <sup>s</sup> 617	+00°33'34"10	20.30	0.3751	4	...	✓	0.55
272	2	03 <sup>h</sup> 20 <sup>m</sup> 27 <sup>s</sup> 678	+00°33'35"89	20.21	0.3750	4	...	✓	0.56
375	2	03 <sup>h</sup> 20 <sup>m</sup> 31 <sup>s</sup> 666	+00°30'03"86	20.37	0.1947	4	✓	...	...
387	3	03 <sup>h</sup> 20 <sup>m</sup> 32 <sup>s</sup> 391	+00°30'03"50	20.12	0.3807	4	...	✓	0.61
14	S	03 <sup>h</sup> 20 <sup>m</sup> 23 <sup>s</sup> 826	+00°33'23"52	20.00	0.3853	4	...	✓	0.66
262	2	03 <sup>h</sup> 20 <sup>m</sup> 27 <sup>s</sup> 178	+00°33'55"14	21.92	0.4733	3	✓	...	...
329	1	03 <sup>h</sup> 20 <sup>m</sup> 29 <sup>s</sup> 739	+00°29'38"15	21.15	0.3848	4	...	✓	0.71
351	2	03 <sup>h</sup> 20 <sup>m</sup> 30 <sup>s</sup> 469	+00°29'35"85	21.94	0.3826	4	✓	✓	0.72
419	3	03 <sup>h</sup> 20 <sup>m</sup> 33 <sup>s</sup> 764	+00°29'47"60	22.29	0.3736	4	✓	✓	0.73
249	2	03 <sup>h</sup> 20 <sup>m</sup> 26 <sup>s</sup> 460	+00°29'21"87	22.22	0.3260	4	✓	...	...
348	1	03 <sup>h</sup> 20 <sup>m</sup> 30 <sup>s</sup> 356	+00°34'47"85	20.64	0.3936	4	...	✓	0.91
19	S	03 <sup>h</sup> 20 <sup>m</sup> 17 <sup>s</sup> 731	+00°31'49"72	19.30	0.3851	4	...	✓	0.94
4	S	03 <sup>h</sup> 20 <sup>m</sup> 27 <sup>s</sup> 081	+00°28'57"99	20.01	0.3905	4	...	✓	0.94
427	3	03 <sup>h</sup> 20 <sup>m</sup> 34 <sup>s</sup> 181	+00°34'56"24	19.36	0.3250	4	...	...	...
364	1	03 <sup>h</sup> 20 <sup>m</sup> 31 <sup>s</sup> 016	+00°28'32"55	19.95	0.3911	4	...	...	...
98	1	03 <sup>h</sup> 20 <sup>m</sup> 16 <sup>s</sup> 227	+00°32'05"75	21.33	0.3690	4	...	...	...
236	2	03 <sup>h</sup> 20 <sup>m</sup> 25 <sup>s</sup> 752	+00°28'40"00	20.47	0.3896	4	...	...	...
246	2	03 <sup>h</sup> 20 <sup>m</sup> 26 <sup>s</sup> 385	+00°28'21"69	22.24	0.3929	4	✓	...	...
199	1	03 <sup>h</sup> 20 <sup>m</sup> 23 <sup>s</sup> 492	+00°35'13"97	21.79	0.4833	4	✓	...	...
411	2	03 <sup>h</sup> 20 <sup>m</sup> 33 <sup>s</sup> 504	+00°35'32"84	18.59	0.1830	4	...	...	...
252	3	03 <sup>h</sup> 20 <sup>m</sup> 26 <sup>s</sup> 596	+00°35'39"38	18.38	0.1958	4	...	...	...

galaxies with gaps of greater than  $1000 \text{ km s}^{-1}$  compared to their neighbour until the number of galaxies in the cluster remains constant. Any galaxies with projected distance from the cluster centre coordinates greater than  $R_{200c}$  (the radius within which the mean density is 200 times the critical density of the Universe), were not considered to be associated with the cluster and therefore rejected. Note that we relate velocity dispersion to cluster mass  $M_{200c}$  using a scaling relation, and calculate  $R_{200c}$  accordingly (assuming spherical symmetry; see Section 3.3 below).

Galaxies flagged as members of ACT-CL J0320.4+0032 are indicated in Table 2; equivalent tables for the other clusters targeted in our SALT observations can be found in the Appendix.

Over all masks, 47 per cent of all successful ( $Q \geq 3$ ) redshift measurements were of galaxies identified as cluster members by the above procedure.

### 3.3 Determining velocity dispersion and mass

We used the biweight scale estimator (described in Beers et al. 1990) to calculate the cluster velocity dispersion  $\sigma_v$  from the galaxies selected as members. Similarly to Sifón et al. (2013), we convert our velocity dispersion measurements into estimates of dynamical mass by applying a scaling relation measured in cosmological simulations. Sifón et al. (2013) used the relation of Evrard et al. (2008), derived from dark matter only simulations, for this purpose. This assumes that galaxy velocities follow the same relation as dark matter particles in  $N$ -body simulations. However, it has been shown (e.g., Carlberg 1994; Colín et al. 2000) that the velocity of subhalos is biased with respect to the dark matter. So, instead we adopt the relation of Munari et al. (2013), which was calibrated using subha-

**Table 3.** Velocity dispersions and derived mass estimates (see Section 3.3) for ACT clusters observed with SALT. The quantities  $M_{500c}$ ,  $R_{500c}$  have been rescaled from  $M_{200c}$ ,  $R_{200c}$  assuming the appropriate relation of Duffy et al. (2008). The Members column gives the total number of members for each cluster; the number of square brackets is the number of these members with redshifts from SDSS DR10. The  $Y_{500c}$  values are rescaled from the values in Hasselfield et al. (2013) for consistency with  $R_{500c}$  as determined from the dynamical mass. We do not report a dynamical mass measurement for ACT-CL J0156.4-0123 as only five members were identified.

Cluster ID	Members [DR10]	$z$	$\sigma_v$ (km s <sup>-1</sup> )	$R_{200c}$ (Mpc)	$M_{200c}$ (10 <sup>14</sup> M <sub>⊙</sub> )	$R_{500c}$ (Mpc)	$M_{500c}$ (10 <sup>14</sup> M <sub>⊙</sub> )	$Y_{500c}$ (10 <sup>-4</sup> arcmin <sup>2</sup> )
ACT-CL J0320.4+0032	27 [5]	0.3838	1430 ± 160	2.3	20.0 ± 5.7	1.4	12.7 ± 3.6	5.7 ± 2.0
ACT-CL J0348.6-0028	22 [0]	0.3451	870 ± 160	1.5	5.1 ± 1.8	0.9	3.4 ± 1.2	2.6 ± 1.2
ACT-CL J0342.7-0017	16 [7]	0.3069	1060 ± 170	1.8	9.1 ± 3.6	1.2	5.9 ± 2.3	4.3 ± 2.0
ACT-CL J2058.8+0123	14 [0]	0.3273	940 ± 120	1.6	6.4 ± 2.1	1.0	4.2 ± 1.4	6.4 ± 2.2
ACT-CL J0219.9+0129	13 [5]	0.3655	900 ± 210	1.5	5.6 ± 3.9	1.0	3.7 ± 2.6	2.6 ± 1.9
ACT-CL J0045.2-0152	13 [4]	0.5492	1020 ± 250	1.5	7.2 ± 4.2	1.0	4.7 ± 2.7	4.1 ± 2.5
ACT-CL J0156.4-0123	5 [1]	0.4559	...	...	...	...	...	...

los and galaxies,

$$\sigma_v \text{ (km s}^{-1}\text{)} = A \left( \frac{0.7 \times E(z) M_{200}}{10^{15} M_{\odot}} \right)^{\alpha}, \quad (2)$$

where  $A = (1177 \pm 4.2) \text{ km s}^{-1}$ ,  $\alpha = 0.364 \pm 0.0021$  and  $E(z) = \sqrt{\Omega_m(1+z)^3 + \Omega_\Lambda}$  (the factor of 0.7 accounts for the assumption of  $H_0 = 70 \text{ km s}^{-1} \text{ Mpc}^{-1}$  in this work). The parameters  $A$  and  $\alpha$  are the normalisation and slope of the relation Munari et al. (2013) obtained from a cosmological hydrodynamical simulation including a model for AGN feedback, using galaxies (with stellar masses  $> 3 \times 10^9 M_{\odot}$ ) as the velocity tracers (see their Table 1). In comparison to the Evrard et al. (2008) relation used in Sifón et al. (2013), equation (2) results in masses which are 16 – 26 per cent smaller for a given velocity dispersion. This is due to dynamical friction and tidal disruption and mergers, which act on galaxies but not on dark matter particles (Munari et al. 2013). This issue will be discussed in detail in the context of the ACT sample, with reference to numerical simulations, in Sifón et al., in preparation.

For convenience, and comparison with other results, we convert our  $M_{200c}$  estimates into  $M_{500c}$ , following the appropriate  $c - M$  relation given in Duffy et al. (2008). We estimated uncertainties on all cluster properties by bootstrap resampling 5000 times.

### 3.4 Cluster properties

Table 3 lists the properties we have measured for each cluster, i.e., number of members, redshift  $z$ , velocity dispersion  $\sigma_v$ , dynamical mass  $M_{200c}$  ( $M_{500c}$ ) and associated radius  $R_{200c}$  ( $R_{500c}$ ), and SZ Comptonisation parameter  $Y_{500c}$ . The latter have been rescaled from the values listed in Hasselfield et al. (2013) to  $R_{500c}$  as determined from the dynamical masses, and we also account for the fractional error on the dynamical mass in the quoted uncertainty on these rescaled  $Y_{500c}$  measurements. The clusters range in  $M_{200c}$  from  $(5.1 - 20.0) \times 10^{14} M_{\odot}$  and span the redshift range  $0.3 < z < 0.55$ . We report spectroscopic redshifts for the first time in the cases of ACT-CL J0156.4-0123 and ACT-CL J2058.8+0123. These new redshift measurements are in excellent agreement with the photometric redshift estimates for these systems recorded in Menanteau et al. (2013). Note that we do not report a velocity dispersion measurement and dynamical mass for J0156.4-0123, as only 5 spectroscopic members were identified in our observations.

## 4 DISCUSSION

### 4.1 Previous measurements of the SZ $Y$ -mass relation

As noted in Section 3.3, in deriving dynamical mass estimates of the clusters observed with SALT we have followed the approach of Sifón et al. (2013), who observed 16 southern ACT clusters with Gemini and the VLT. However, in this work we have adopted the scaling relation of Munari et al. (2013), rather than Evrard et al. (2008), for the conversion of velocity dispersion into mass. We present a comparison of the SALT clusters to the Sifón et al. (2013) sample in the  $Y_{500c} - M_{500c}$  plane in Fig. 3; note the  $M_{200c}$  measurements for all clusters have been converted to  $M_{500c}$  using the  $c - M$  relation of Duffy et al. (2008), and the  $Y_{500c}$  measurements have been rescaled from those reported in Hasselfield et al. (2013) to  $R_{500c}$  as determined from the dynamical masses.

As can be seen in Fig. 3, the ACT clusters observed with SALT occupy the same region of the  $Y_{500c} - M_{500c}$  plot as the Sifón et al. (2013) sample, after converting the velocity dispersions reported in Sifón et al. (2013) to masses using the Munari et al. (2013) scaling relation and rescaling the  $Y_{500c}$  measurements appropriately. Also plotted in Fig. 3 are some recent  $Y_{500c} - M_{500c}$  relations from the literature: the baseline mass calibration adopted in the Planck Collaboration (2013) cosmological study (calibrated from X-ray observations, and here we assume the hydrostatic bias parameter  $b = 0.2$ ); the relation of Marrone et al. (2012), derived from Sunyaev-Zel'dovich Array (SZA) observations of Local Cluster Substructure Survey (LoCuSS) clusters, which have mass estimates from gravitational weak lensing (Okabe et al. 2010); and the relation of Andersson et al. (2011), with masses measured from *Chandra* and *XMM-Newton* observations of South Pole Telescope clusters (Vanderlinde et al. 2010).

We find that with the adoption of the Munari et al. (2013) scaling relation, the ACT clusters scatter around the relations measured by Planck Collaboration (2013) and Andersson et al. (2011), which are both derived from X-ray observations (note however that in this work we do not correct for Malmquist-like flux bias as was done in Sifón et al. 2013; the size of this correction is less than 10 per cent for most clusters in the Sifón et al. 2013 sample, rising to 20 per cent in the case of the lowest mass cluster, ACT-CL J0509-5341). The data have a higher normalisation than is found in the weak-lensing based SZA/LoCuSS measurement (Marrone et al. 2012). If we had instead used the Evrard et al. (2008)  $\sigma_v - M_{200}$  scaling, the dynamical mass measurements would be 16 – 26 per cent higher, causing the majority of the ACT clusters to lie above all of these recent scaling relation measurements. Such a bias in the scal-



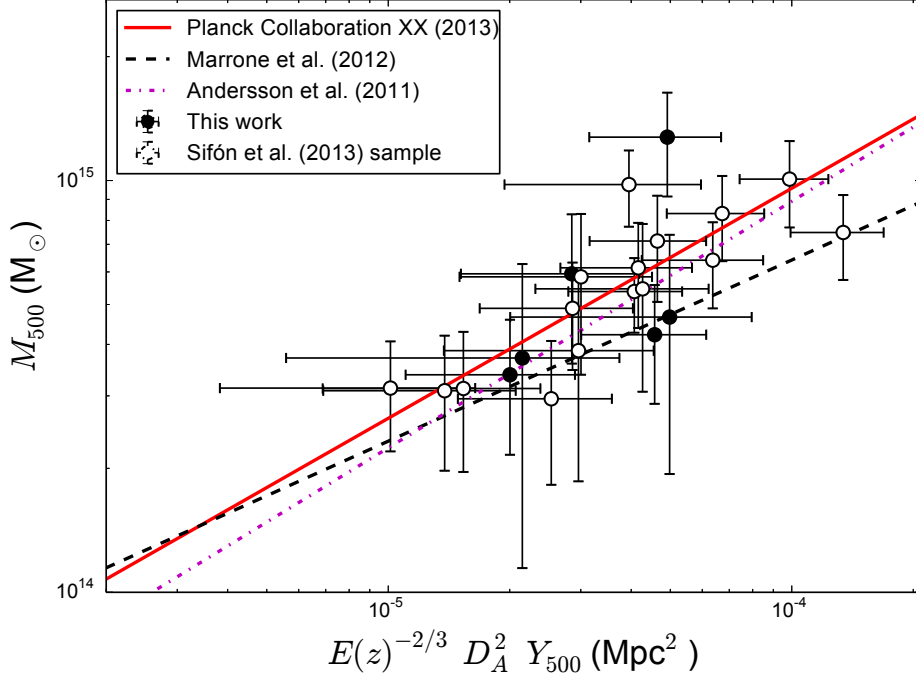


**Figure 3.** Comparison of SALT-derived dynamical masses for ACT equatorial clusters (labelled ‘this work’) and the sample of Sifón et al. (2013), who obtained such measurements for the ACT southern sample (Menanteau et al. 2010; Marriage et al. 2011). Here all masses (including those of clusters in the Sifón et al. 2013 sample) have been obtained from velocity dispersions using the Munari et al. (2013) scaling relation, rather than the Evrard et al. (2008) scaling relation assumed in Sifón et al. (2013). All  $Y_{500c}$  measurements shown have been rescaled to apertures consistent with  $R_{500c}$  determined from the dynamical masses. We also show recent  $Y_{500c} - M_{500c}$  scaling relations from the literature for comparison: the solid line shows the fiducial relation adopted in Planck Collaboration (2013) with hydrostatic mass bias  $(1 - b) = 0.8$  (here the masses are derived from X-ray observations); the dashed line shows the relation measured by Marrone et al. (2012) from SZA observations of LoCuSS clusters at  $z \approx 0.2$ , where the masses are measured from weak gravitational lensing; and the dot-dashed line shows the relation of Andersson et al. (2011), derived from X-ray observations of SPT clusters (Vanderlinde et al. 2010). The SALT dynamical masses appear to be drawn from the same distribution as Sifón et al. (2013). With the adoption of the Munari et al. (2013) scaling relation for conversion of velocity dispersion into mass, we see the ACT clusters are consistent with the Planck Collaboration (2013) and Andersson et al. (2011)  $Y_{500c} - M_{500c}$  relations, though have a higher normalisation than the Marrone et al. (2012) relation.

ing relation normalisation would lead to larger inferred values for  $\sigma_8$  (the normalisation of the dark matter power spectrum) and  $\Omega_m$  in a cosmological analysis (see, e.g., the discussion in Hasselfield et al. 2013, where the impact of various different scaling relation assumptions is considered). This issue will be discussed in detail, with reference to results from cosmological simulations, in Sifón et al. (in prep.), which will present an updated fit to the  $Y_{500c} - M_{500c}$  relation using the full sample of 48 ACT clusters with velocity dispersion measurements from the literature, Gemini, SALT, and the VLT.

The cluster which deviates most from the southern ACT sample is ACT-CL J0320.4+0032 (the most massive cluster in this study), which has a somewhat lower  $Y_{500c}$  than expected given its mass. Based on the uncertainty in its dynamical mass, it deviates from the Planck Collaboration (2013)  $Y_{500c} - M_{500c}$  scaling relation by  $1.8\sigma$ . If this has a physical (rather than statistical) cause, it could be due to substructure in the line of sight velocity distribution; this could lead to an overestimate of the velocity dispersion, and in turn the dynamical mass. More spectroscopic members need to be identified in order to test if this is the case. Alternatively, we know that the BCG of this cluster is a quasar host, and it may be possible that recent AGN activity has had some influence on the intracluster medium (ICM), and hence the SZ signal, although more data are needed to investigate this.

## 4.2 ACT-CL J0320.4+0032: a Type II quasar hosted in a Brightest Cluster Galaxy

As seen in Fig. 1 and noted in Section 2.4, the BCG in ACT-CL J0320.4+0032 has relatively broad emission lines, indicating AGN activity. This object has previously been identified as a candidate Type II quasar (i.e., an obscured AGN) in the catalogue of Zakamska et al. (2003), on the basis of the equivalent width of the  $[\text{OIII}]\lambda 5007$  line in its SDSS spectrum, and was subsequently observed with the *Hubble Space Telescope* in November 2006 (PI: H. Schmitt, HST Proposal 10880). Villar-Martín et al. (2012) conducted a study of the morphologies of Type II AGN hosts using these data, finding that the host galaxy (SDSS J032029.78+003153.5 in their catalogue) is an elliptical with a somewhat disturbed morphology, and possibly a double nucleus. Ramos Almeida et al. (2013) identified this object as being in a clustered environment, but did not note that the host galaxy is actually the BCG of a massive cluster. The object is not detected as a 1.4 GHz source in either FIRST (Faint Images of the Radio Sky at Twenty-cm; Becker et al. 1995) or NVSS (National Radio Astronomy Observatory Very Large Array Sky Survey; Condon et al. 1998).

The active BCG of ACT-CL J0320.4+0032 is a rare discovery, since only a handful of BCGs are known to host Type II



quasars. The other examples are IRAS 09104+4109 (Kleinmann et al. 1988; O’Sullivan et al. 2012), Cygnus A (Antonucci et al. 1994), Zw8029 (Russell et al. 2013), and the recent discovery that the central galaxy of the Phoenix Cluster at  $z = 0.596$  is a Type II quasar (Ueda et al. 2013). In the latter case, the quasar has evidently not yet stemmed the cooling of gas, as the central galaxy is also undergoing a starburst (McDonald et al. 2012, 2014). In addition, some other BCG quasar hosts (NGC 1275, 4C+55.16, 1H1821+644), all located in cool core clusters, have similar line ratios to ACT-CL J0320.4+0032, although they are not formally classified as Type II quasars (A. Edge, private communication).

The study of such rare systems is important for quantifying the effect of quasar-mode feedback on the ICM (see the review by Fabian 2012). It is well established that radio jets, triggered by radiatively inefficient, low levels of accretion onto supermassive black holes in BCGs, carve out cavities in the ICM (e.g., McNamara et al. 2005; Hlavacek-Larrondo et al. 2013); indeed, this is the main evidence we have for the influence of AGN activity on large scales. The gas that fuels radio mode AGN is thought to originate in the hot intracluster material, as supported by recent analyses indicating that radio AGN inhabit environments that support hot atmospheres (Gralla et al. 2014). Quasar-mode feedback, on the other hand, is radiatively efficient, associated with high accretion rates, drives ubiquitous winds (with velocities  $\sim 800 \text{ km s}^{-1}$ ; McElroy et al. 2014), and is thought to be responsible for the quenching of star formation in massive galaxies (e.g., Di Matteo et al. 2005; Croton et al. 2006; Bower et al. 2006). Evolution is expected from the quasar-mode to radio-mode (e.g., Churazov et al. 2005), with the former including a highly obscured stage that keeps the quasar hidden from view in the optical (e.g., Hopkins et al. 2005). Sometimes, radio-emitting bubbles are seen in association with Type II quasars, as in the case of the Teacup AGN (Harrison et al. 2014).

Therefore, with only a couple of other similar systems known, ACT-CL J0320.4+0032 may be an important system to study, in order to understand the evolution between these modes of feedback in very massive haloes. As noted above, the SZ signal for ACT-CL J0320.4+0032 is relatively low given its dynamical mass, although only at the  $1.8\sigma$  level. In a study investigating radio-mode feedback, Gralla et al. (2014) found that the SZ effect associated with radio AGN host haloes is somewhat lower than expected from SZ-mass scaling relations. The possibility of suppression of the SZ signal by AGN feedback in this cluster (perhaps from previous radio-mode feedback episodes) could be investigated using X-ray observations (there are no data on this object in the *Chandra* or *XMM-Newton* archives), through measuring the cluster mass with X-ray proxies, and searching for evidence of cavities in the X-ray emission. If seen, this would indicate a previous radio-mode feedback episode. With regards to other Type II quasars hosted in cluster BCGs, we note that some evidence for cavities has recently been reported on the basis of *Chandra* observations of the Phoenix cluster (Hlavacek-Larrondo et al. 2014), but no cavities have yet been identified in IRAS 09104+4109 (Hlavacek-Larrondo et al. 2013). In performing such a study, care must be taken to separate the emission of the quasar from the cluster signal. Such observations, when combined with optical spectroscopy, can also be used to measure the obscuration of the nucleus (e.g., Jia et al. 2013). Spatially resolved spectroscopic observations may also be used to investigate outflows from the quasar (e.g., Villar-Martín et al. 2012; McDonald et al. 2014; McElroy et al. 2014).

## 5 SUMMARY

We have conducted a pilot program of spectroscopic follow-up observations of galaxy clusters discovered via the SZ effect, by ACT in its equatorial strip survey, using the RSS instrument on SALT. We successfully measured secure redshifts for 191 out of 372 galaxies (overall 51 per cent efficiency) in 7 cluster fields, targeting galaxies with  $r$ -band magnitudes in the range 17.9–23.9, with between 1950–3900 sec of exposure time.

We measured the redshifts, velocity dispersions, and estimated dynamical masses of the clusters. We made the first spectroscopic redshift measurements for two systems, ACT-CL J0156.4-0123 ( $z = 0.456$ ) and ACT-CL J2058.8+0123 ( $z = 0.327$ ), finding these to be in excellent agreement with the photometric redshift estimates presented in Menanteau et al. (2013). Using a scaling relation from the cosmological hydrodynamical simulations of Munari et al. (2013) to convert velocity dispersion into mass, we found that the clusters range in mass ( $M_{200c}$ ) from  $(5 - 20) \times 10^{14} M_{\odot}$ . The previous study of ACT cluster dynamical masses (Sifón et al. 2013), used the Evrard et al. (2008) scaling relation, based on the results of dark matter only simulations, to convert velocity dispersion into mass. The Munari et al. (2013)-based masses are 16 – 26 per cent smaller. We found that the SALT clusters occupy a similar region of the  $Y_{500c} - M_{500c}$  plane to the Sifón et al. (2013) sample, and that they are in good agreement with recent measurements of the  $Y_{500c} - M_{500c}$  relation measured based on X-ray observations. The ACT clusters are slightly more massive on average than would be expected if the Marrone et al. (2012) weak-lensing based  $Y_{500c} - M_{500c}$  relation is used for comparison. A future study (Sifón et al., in prep.) of the complete sample of 48 ACT clusters with dynamical mass measurements from Gemini, SALT, and the VLT will present an updated measurement of the  $Y_{500c} - M_{500c}$  relation, and consider in detail the potential sources of bias in the observational measurements through comparison with the results of numerical simulations.

In conducting this study, we also found that the BCG in ACT-CL J0320.4+0032 is host to a previously identified Type II quasar (Zakamska et al. 2003; Villar-Martín et al. 2012). However, these previous studies were not aware that this object is located in a massive cluster of galaxies, and it is one of only a handful of such systems that have been discovered. Further follow-up observations of this object may help to illuminate the role played by quasar-mode feedback in massive clusters.

Overall, this study has proved to be a successful early use of SALT for extragalactic astronomy. These results, as well as continued efforts to improve the telescope and instrument performance, justify a more extensive use of SALT in the future for exploring higher  $z$  clusters, such as those that are being discovered with ACT-Pol (Naess et al. 2014).

## ACKNOWLEDGMENTS

We thank the anonymous referee for a number of suggestions that improved the quality of this paper. We thank Alastair Edge for useful discussions about known BCG quasar hosts. This work is based in large part on observations obtained with the Southern African Large Telescope (SALT). Funding for SALT is provided in part by Rutgers University, a founding member of the SALT consortium. BK, MHi and KM acknowledge financial support from the National Research Foundation and the University of KwaZulu-Natal. This work was supported by the U.S. National Science Foundation through awards AST-0408698 and AST-0965625 for the

ACT project, as well as awards PHY-0855887 and PHY-1214379, along with awards AST-0955810 to AJB and AST-1312380 to AK. Funding was also provided by Princeton University, the University of Pennsylvania, and a Canada Foundation for Innovation (CFI) award to UBC. ACT operates in the Parque Astronómico Atacama in northern Chile under the auspices of the Comisión Nacional de Investigación Científica y Tecnológica (CONICYT). Computations were performed on the GPC supercomputer at the SciNet HPC Consortium. SciNet is funded by the CFI under the auspices of Compute Canada, the Government of Ontario, the Ontario Research Fund – Research Excellence; and the University of Toronto. Funding for SDSS-III has been provided by the Alfred P. Sloan Foundation, the Participating Institutions, the National Science Foundation, and the U.S. Department of Energy Office of Science. The SDSS-III web site is <http://www.sdss3.org/>. SDSS-III is managed by the Astrophysical Research Consortium for the Participating Institutions of the SDSS-III Collaboration (see the SDSS-III web site for details).

## REFERENCES

- Abazajian K. N., Adelman-McCarthy J. K., Agüeros M. A., Allam S. S., Allende Prieto C., An D., Anderson K. S. J., Anderson S. F., Annis J., Bahcall N. A., et al. 2009, *ApJS*, 182, 543
- Ahn C. P., Alexandroff R., Allende Prieto C., Anders F., Anderson S. F., Anderton T., Andrews B. H., Aubourg É., Bailey S., Bastien F. A., et al. 2014, *ApJS*, 211, 17
- Aihara H., et al., 2011, *ApJS*, 193, 29
- Andersson K., et al., 2011, *ApJ*, 738, 48
- Annis J., et al., 2011, *ApJ* submitted (arXiv:1111.6619)
- Antonucci R., Hurt T., Kinney A., 1994, *Nature*, 371, 313
- Becker R. H., White R. L., Helfand D. J., 1995, *ApJ*, 450, 559
- Beers T. C., Flynn K., Gebhardt K., 1990, *AJ*, 100, 32
- Benson B. A., et al., 2013, *ApJ*, 763, 147
- Birkinshaw M., 1999, *Physics Reports*, 310, 97
- Bleem L. E., et al., 2014, *ApJ* submitted (arXiv:1409.0850)
- Bocquet S., et al., 2014, *ApJ* submitted (arXiv:1407.2942)
- Bower R. G., Benson A. J., Malbon R., Helly J. C., Frenk C. S., Baugh C. M., Cole S., Lacey C. G., 2006, *MNRAS*, 370, 645
- Buckley D. A. H., Swart G. P., Meiring J. G., 2006, in *Society of Photo-Optical Instrumentation Engineers (SPIE) Conference Series Vol. 6267 of Society of Photo-Optical Instrumentation Engineers (SPIE) Conference Series, Completion and commissioning of the Southern African Large Telescope*
- Burgh E. B., Nordsieck K. H., Kobulnicky H. A., Williams T. B., O'Donoghue D., Smith M. P., Percival J. W., 2003, in *Iye M., Moorwood A. F. M., eds, Society of Photo-Optical Instrumentation Engineers (SPIE) Conference Series Vol. 4841 of Society of Photo-Optical Instrumentation Engineers (SPIE) Conference Series, Prime Focus Imaging Spectrograph for the Southern African Large Telescope: optical design. pp 1463–1471*
- Carlberg R. G., 1994, *ApJ*, 433, 468
- Carlstrom J. E., Holder G. P., Reese E. D., 2002, *ARA&A*, 40, 643
- Catala L., Crawford S. M., Buckley D. A. H., Pickering T. E., Wilson R. W., Butterley T., Shepherd H. W., Marang F., Matshaya P., Fourie C., 2013, *MNRAS*, 436, 590
- Churazov E., Sazonov S., Sunyaev R., Forman W., Jones C., Böhringer H., 2005, *MNRAS*, 363, L91
- Colín P., Klypin A. A., Kravtsov A. V., 2000, *ApJ*, 539, 561
- Condon J. J., Cotton W. D., Greisen E. W., Yin Q. F., Perley R. A., Taylor G. B., Broderick J. J., 1998, *AJ*, 115, 1693
- Crawford S. M., Still M., Schellart P., Balona L., Buckley D. A. H., Dugmore G., Gulbis A. A. S., Kniazev A., Kotze M., Loaring N., Nordsieck K. H., Pickering T. E., Potter S., Romero Colmenero E., Vaisanen P., Williams T., Zietsman E., 2010, in *Society of Photo-Optical Instrumentation Engineers (SPIE) Conference Series Vol. 7737 of Society of Photo-Optical Instrumentation Engineers (SPIE) Conference Series, PySALT: the SALT science pipeline*
- Crawford S. M., Wirth G. D., Bershadsky M. A., 2014, *ApJ*, 786, 30
- Croton D. J., Springel V., White S. D. M., De Lucia G., Frenk C. S., Gao L., Jenkins A., Kauffmann G., Navarro J. F., Yoshida N., 2006, *MNRAS*, 365, 11
- De Propriis R., et al., 2002, *MNRAS*, 329, 87
- Di Matteo T., Springel V., Hernquist L., 2005, *Nature*, 433, 604
- Duffy A. R., Schaye J., Kay S. T., Dalla Vecchia C., 2008, *MNRAS*, 390, L64
- Dünner R., et al., 2013, *ApJ*, 762, 10
- Evrard A. E., Bialek J., Busha M., White M., Habib S., Heitmann K., Warren M., Rasia E., Tormen G., Moscardini L., Power C., Jenkins A. R., Gao L., Frenk C. S., Springel V., White S. D. M., Diemand J., 2008, *ApJ*, 672, 122
- Fabian A. C., 2012, *ARA&A*, 50, 455
- Fadda D., Girardi M., Giuricin G., Mardirossian F., Mezzetti M., 1996, *apj*, 473, 670
- Gralla M. B., et al., 2014, *MNRAS*, 445, 460
- Harrison C. M., Thomson A. P., Alexander D. M., Bauer F. E., Edge A. C., Hogan M. T., Mullaney J. R., Swinbank A. M., 2014, *ApJ* submitted (arXiv:1410.4198)
- Hasselfield M., et al., 2013, *JCAP*, 7, 8
- Hlavacek-Larrondo J., et al., 2014, *ApJ* submitted (arXiv:1410.0025)
- Hlavacek-Larrondo J., Fabian A. C., Edge A. C., Ebeling H., Allen S. W., Sanders J. S., Taylor G. B., 2013, *MNRAS*, 431, 1638
- Hoekstra H., Mahdavi A., Babul A., Bildfell C., 2012, *MNRAS*, 427, 1298
- Hopkins P. F., Hernquist L., Martini P., Cox T. J., Robertson B., Di Matteo T., Springel V., 2005, *ApJL*, 625, L71
- Jia J., Ptak A., Heckman T., Zakamska N. L., 2013, *ApJ*, 777, 27
- Kleinmann S. G., Hamilton D., Keel W. C., Wynn-Williams C. G., Eales S. A., Becklin E. E., Kuntz K. D., 1988, *ApJ*, 328, 161
- Kurtz M. J., Mink D. J., 1998, *PASP*, 110, 934
- Mantz A., Allen S. W., Rapetti D., Ebeling H., 2010, *MNRAS*, 406, 1759
- Marriage T. A., et al., 2011, *ApJ*, 737, 61
- Marrone D. P., Smith G. P., Okabe N., Bonamente 2012, *apj*, 754, 119
- McDonald M., et al., 2012, *Nature*, 488, 349
- McDonald M., Swinbank M., Edge A. C., Wilner D. J., Veilleux S., Benson B. A., Hogan M. T., Marrone D. P., McNamara B. R., Wei L. H., Bayliss M. B., Bautz M. W., 2014, *ApJ*, 784, 18
- McElroy R., Croom S. M., Pracy M., Sharp R., Ho I., Medling A. M., 2014, *MNRAS* in press (arXiv:1410.6552)
- McNamara B. R., Nulsen P. E. J., Wise M. W., Rafferty D. A., Carilli C., Sarazin C. L., Blanton E. L., 2005, *Nature*, 433, 45
- Menanteau F., et al., 2010, *ApJ*, 723, 1523
- Menanteau F., et al., 2013, *ApJ*, 765, 67
- Munari E., Biviano A., Borgani S., Murante G., Fabjan D., 2013, *MNRAS*, 430, 2638
- Naess S., et al., 2014, *JCAP* in press (arXiv:1405.5524)

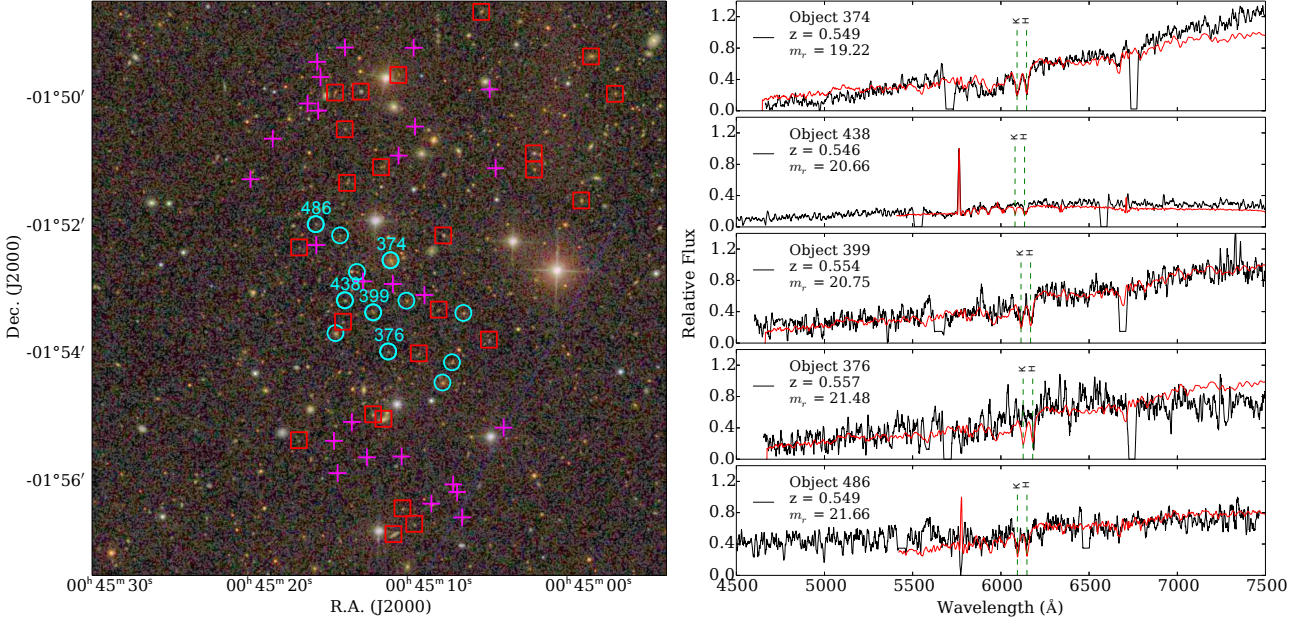
- Okabe N., Takada M., Umetsu K., Futamase T., Smith G. P., 2010, PASJ, 62, 811
- Oke J. B., 1974, ApJS, 27, 21
- O’Sullivan E., Giacintucci S., Babul A., Raychaudhury S., Venturi T., Bildfell C., Mahdavi A., Oonk J. B. R., Murray N., Hoekstra H., Donahue M., 2012, MNRAS, 424, 2971
- Planck Collaboration 2013, A&A in press, arXiv:1303.5080
- Planck Collaboration Ade P. A. R., Aghanim N., Armitage-Caplan C., Arnaud M., Ashdown M., Atrio-Barandela F., Aumont J., Aussel H., Baccigalupi C., et al. 2013, ArXiv e-prints
- Planck Collaboration Ade P. A. R., Aghanim N., Arnaud M., Ashdown M., Aumont J., Baccigalupi C., Balbi A., Banday A. J., Barreiro R. B., et al. 2011, A&A, 536, A11
- Ramos Almeida C., Bessiere P. S., Tadhunter C. N., Inskip K. J., Morganti R., Dicken D., González-Serrano J. I., Holt J., 2013, MNRAS, 436, 997
- Reichardt C. L., et al., 2013, ApJ, 763, 127
- Rozo E., et al., 2009, ApJ, 699, 768
- Russell H. R., McNamara B. R., Edge A. C., Hogan M. T., Main R. A., Vantyghem A. N., 2013, MNRAS, 432, 530
- Sehgal N., et al., 2011, ApJ, 732, 44
- Sifón C., Menanteau F., Hasselfield M., et al., 2013, ApJ, 772, 25
- Staniszewski Z., et al., 2009, ApJ, 701, 32
- Sunyaev R. A., Zel’dovich Y. B., 1970, Comments on Astrophysics and Space Physics, 2, 66
- Swetz D. S., et al., 2011, ApJS, 194, 41
- Ueda S., Hayashida K., Anabuki N., Nakajima H., Koyama K., Tsunemi H., 2013, ApJ, 778, 33
- Vanderlinde K., et al., 2010, ApJ, 722, 1180
- Vikhlinin A., et al., 2009, ApJ, 692, 1060
- Vikhlinin A., Kravtsov A., Forman W., Jones C., Markevitch M., Murray S. S., Van Speybroeck L., 2006, ApJ, 640, 691
- Villar-Martín M., Cabrera Lavers A., Bessiere P., Tadhunter C., Rose M., de Breuck C., 2012, MNRAS, 423, 80
- Wirth G. D., Willmer C. N. A., Amico e. a., 2004, aj, 127, 3121
- Zakamska N. L., Strauss M. A., Krolik J. H., Collinge M. J., Hall P. B., Hao L., Heckman T. M., Ivezić Ž., Richards G. T., Schlegel D. J., Schneider D. P., Strateva I., Vanden Berk D. E., Anderson S. F., Brinkmann J., 2003, AJ, 126, 2125

## APPENDIX

The tables below list the spectroscopic redshifts measured with SALT RSS in each ACT cluster field. We also present a selection of images and spectra in the same style as Fig. 1.

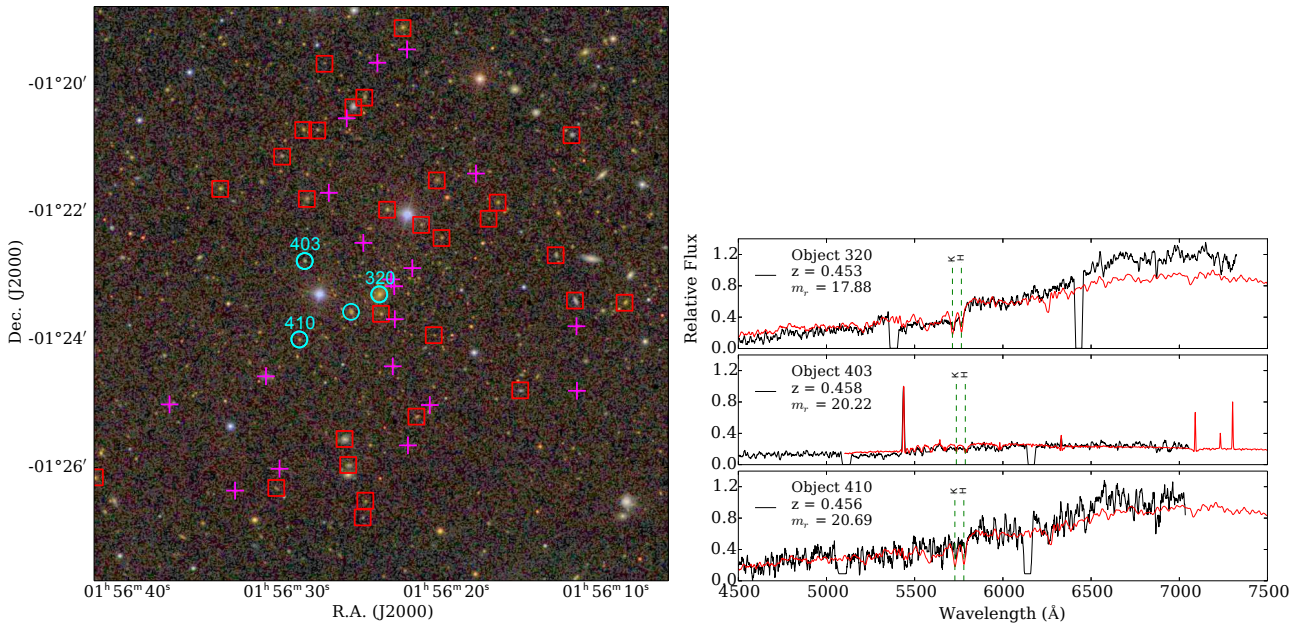
**Table A1.** Spectroscopic redshifts of galaxies in the direction of ACT-CL J0045.2-0152 measured using SALT RSS; see Table 2 for an explanation of the table columns.

ID	Mask	RA (J2000)	Dec. (J2000)	$m_r$	$z$	$Q$	Em. Lines?	Member?	$r$ (Mpc)
374	1	00 <sup>h</sup> 45 <sup>m</sup> 12 <sup>s</sup> .499	−01°52′31″.65	19.22	0.5486	4	...	✓	0.00
418	1	00 <sup>h</sup> 45 <sup>m</sup> 14 <sup>s</sup> .607	−01°52′42″.69	21.98	0.5482	4	...	✓	0.21
18	S	00 <sup>h</sup> 45 <sup>m</sup> 11 <sup>s</sup> .507	−01°53′09″.64	20.66	0.5404	4	...	✓	0.26
399	1	00 <sup>h</sup> 45 <sup>m</sup> 13 <sup>s</sup> .586	−01°53′20″.61	20.75	0.5543	4	✓	✓	0.33
446	1	00 <sup>h</sup> 45 <sup>m</sup> 15 <sup>s</sup> .661	−01°52′08″.31	21.99	0.5504	4	...	✓	0.34
438	1	00 <sup>h</sup> 45 <sup>m</sup> 15 <sup>s</sup> .359	−01°53′09″.28	20.66	0.5457	4	✓	✓	0.37
306	2	00 <sup>h</sup> 45 <sup>m</sup> 09 <sup>s</sup> .483	−01°53′17″.99	21.47	0.9898	4	...	...	...
440	2	00 <sup>h</sup> 45 <sup>m</sup> 15 <sup>s</sup> .476	−01°53′29″.43	21.38	0.4880	4	✓	...	...
486	2	00 <sup>h</sup> 45 <sup>m</sup> 17 <sup>s</sup> .187	−01°51′57″.75	21.66	0.5491	4	...	✓	0.50
434	2	00 <sup>h</sup> 45 <sup>m</sup> 15 <sup>s</sup> .222	−01°51′18″.97	21.33	0.5490	3	...	✓	0.53
7	S	00 <sup>h</sup> 45 <sup>m</sup> 07 <sup>s</sup> .935	−01°53′21″.18	20.40	0.5488	4	...	✓	0.54
451	1	00 <sup>h</sup> 45 <sup>m</sup> 15 <sup>s</sup> .949	−01°53′40″.05	19.88	0.5535	4	...	✓	0.55
376	1	00 <sup>h</sup> 45 <sup>m</sup> 12 <sup>s</sup> .645	−01°53′57″.37	21.48	0.5574	3	...	✓	0.55
509	1	00 <sup>h</sup> 45 <sup>m</sup> 18 <sup>s</sup> .228	−01°52′19″.59	21.93	0.7100	4	✓	...	...
387	1	00 <sup>h</sup> 45 <sup>m</sup> 13 <sup>s</sup> .094	−01°51′04″.19	21.45	0.5130	4	✓	...	...
335	2	00 <sup>h</sup> 45 <sup>m</sup> 10 <sup>s</sup> .733	−01°53′59″.12	21.66	0.6379	4	...	...	...
14	S	00 <sup>h</sup> 45 <sup>m</sup> 08 <sup>s</sup> .649	−01°54′07″.50	20.77	0.5526	4	...	✓	0.72
251	2	00 <sup>h</sup> 45 <sup>m</sup> 06 <sup>s</sup> .334	−01°53′46″.27	21.34	0.6425	3	✓	...	...
11	S	00 <sup>h</sup> 45 <sup>m</sup> 09 <sup>s</sup> .245	−01°54′26″.52	20.04	0.5388	4	...	✓	0.80
439	1	00 <sup>h</sup> 45 <sup>m</sup> 15 <sup>s</sup> .372	−01°50′28″.54	21.44	0.6570	4	✓	...	...
400	1	00 <sup>h</sup> 45 <sup>m</sup> 13 <sup>s</sup> .59	−01°54′56″.36	20.47	0.3675	3	...	...	...
415	1	00 <sup>h</sup> 45 <sup>m</sup> 14 <sup>s</sup> .368	−01°49′53″.20	20.15	0.2431	4	✓	...	...
207	1	00 <sup>h</sup> 45 <sup>m</sup> 03 <sup>s</sup> .524	−01°50′51″.21	20.18	0.4726	4	...	...	...
363	1	00 <sup>h</sup> 45 <sup>m</sup> 12 <sup>s</sup> .009	−01°49′37″.58	21.18	0.5434	4	...	...	...
510	2	00 <sup>h</sup> 45 <sup>m</sup> 18 <sup>s</sup> .243	−01°55′20″.68	21.61	0.5284	3	✓	...	...
355	1	00 <sup>h</sup> 45 <sup>m</sup> 11 <sup>s</sup> .751	−01°56′24″.72	21.26	0.5523	4	✓	...	...
343	1	00 <sup>h</sup> 45 <sup>m</sup> 11 <sup>s</sup> .012	−01°56′39″.24	21.58	0.2010	4	...	...	...
371	2	00 <sup>h</sup> 45 <sup>m</sup> 12 <sup>s</sup> .315	−01°56′48″.94	19.37	0.8268	4	...	...	...

**Figure A1.** The  $z = 0.55$  cluster ACT-CL J0045.2-0152 (see Fig. 1 for an explanation of symbols and colours).

**Table A2.** Spectroscopic redshifts of galaxies in the direction of ACT-CL J0156.4-0123 measured using SALT RSS; see Table 2 for an explanation of the table columns.

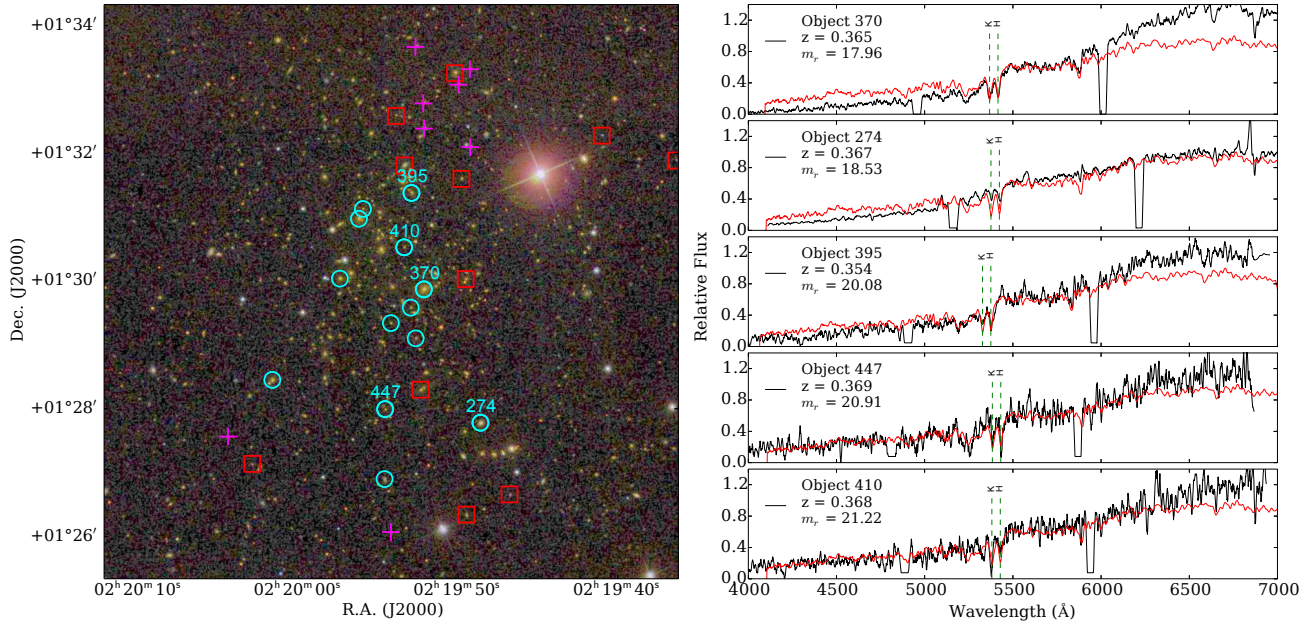
ID	Mask	RA (J2000)	Dec. (J2000)	$m_r$	$z$	$Q$	Em. Lines?	Member?	$r$ (Mpc)
320	1	01 <sup>h</sup> 56 <sup>m</sup> 24 <sup>s</sup> .297	−01°23′17″.32	17.88	0.4526	4	...	✓	0.00
317	1	01 <sup>h</sup> 56 <sup>m</sup> 24 <sup>s</sup> .192	−01°23′35″.61	20.34	0.4380	4	...	...	...
6	S	01 <sup>h</sup> 56 <sup>m</sup> 26 <sup>s</sup> .066	−01°23′33″.76	19.55	0.4602	4	...	✓	0.18
246	3	01 <sup>h</sup> 56 <sup>m</sup> 20 <sup>s</sup> .883	−01°23′55″.64	21.45	0.5965	3	...	...	...
268	1	01 <sup>h</sup> 56 <sup>m</sup> 21 <sup>s</sup> .674	−01°22′12″.07	21.08	0.4435	4	✓	...	...
403	1	01 <sup>h</sup> 56 <sup>m</sup> 28 <sup>s</sup> .970	−01°22′46″.03	20.22	0.4582	4	✓	✓	0.44
239	1	01 <sup>h</sup> 56 <sup>m</sup> 20 <sup>s</sup> .400	−01°22′24″.40	20.78	0.5689	4	...	...	...
310	1	01 <sup>h</sup> 56 <sup>m</sup> 23 <sup>s</sup> .810	−01°21′57″.79	19.71	0.2769	4	...	...	...
410	1	01 <sup>h</sup> 56 <sup>m</sup> 29 <sup>s</sup> .305	−01°23′59″.72	20.69	0.4561	4	...	✓	0.50
243	1	01 <sup>h</sup> 56 <sup>m</sup> 20 <sup>s</sup> .696	−01°21′30″.28	19.90	0.5597	4	✓	✓	0.69
195	3	01 <sup>h</sup> 56 <sup>m</sup> 17 <sup>s</sup> .450	−01°22′06″.30	21.92	0.5985	3	✓	...	...
361	1	01 <sup>h</sup> 56 <sup>m</sup> 26 <sup>s</sup> .472	−01°25′33″.21	18.22	0.1368	4	✓	...	...
186	3	01 <sup>h</sup> 56 <sup>m</sup> 16 <sup>s</sup> .882	−01°21′51″.12	20.06	0.5683	4	...	...	...
419	1	01 <sup>h</sup> 56 <sup>m</sup> 30 <sup>s</sup> .384	−01°21′07″.92	20.60	0.6804	4	✓	...	...
164	1	01 <sup>h</sup> 56 <sup>m</sup> 15 <sup>s</sup> .462	−01°24′47″.50	20.03	0.6058	4	✓	...	...
355	1	01 <sup>h</sup> 56 <sup>m</sup> 26 <sup>s</sup> .243	−01°25′57″.64	19.66	0.3397	4	✓	...	...
393	1	01 <sup>h</sup> 56 <sup>m</sup> 28 <sup>s</sup> .181	−01°20′43″.36	20.68	0.3941	4	...	...	...
142	3	01 <sup>h</sup> 56 <sup>m</sup> 13 <sup>s</sup> .247	−01°22′40″.53	19.98	0.7713	3	✓	...	...
350	3	01 <sup>h</sup> 56 <sup>m</sup> 25 <sup>s</sup> .923	−01°20′21″.53	18.60	0.3808	4	✓	...	...
468	3	01 <sup>h</sup> 56 <sup>m</sup> 34 <sup>s</sup> .261	−01°21′38″.25	19.58	0.3400	4	...	...	...
123	3	01 <sup>h</sup> 56 <sup>m</sup> 12 <sup>s</sup> .040	−01°23′23″.13	19.12	0.4773	4	✓	...	...
337	1	01 <sup>h</sup> 56 <sup>m</sup> 25 <sup>s</sup> .235	−01°20′12″.52	20.15	0.0392	4	...	...	...
335	1	01 <sup>h</sup> 56 <sup>m</sup> 25 <sup>s</sup> .171	−01°26′31″.22	20.65	0.4551	4	...	...	...
426	1	01 <sup>h</sup> 56 <sup>m</sup> 30 <sup>s</sup> .748	−01°26′19″.24	20.93	0.4497	4	...	...	...
340	1	01 <sup>h</sup> 56 <sup>m</sup> 25 <sup>s</sup> .337	−01°26′46″.89	21.09	0.7356	4	✓	...	...
385	3	01 <sup>h</sup> 56 <sup>m</sup> 27 <sup>s</sup> .728	−01°19′40″.68	21.59	0.3845	3	...	...	...
127	3	01 <sup>h</sup> 56 <sup>m</sup> 12 <sup>s</sup> .255	−01°20′47″.78	19.70	0.4215	3	✓	...	...

**Figure A2.** The  $z = 0.46$  cluster ACT-CL J0156.4-0123 (see Fig. 1 for an explanation of symbols and colours) The unlabelled member galaxy is from SDSS DR10.



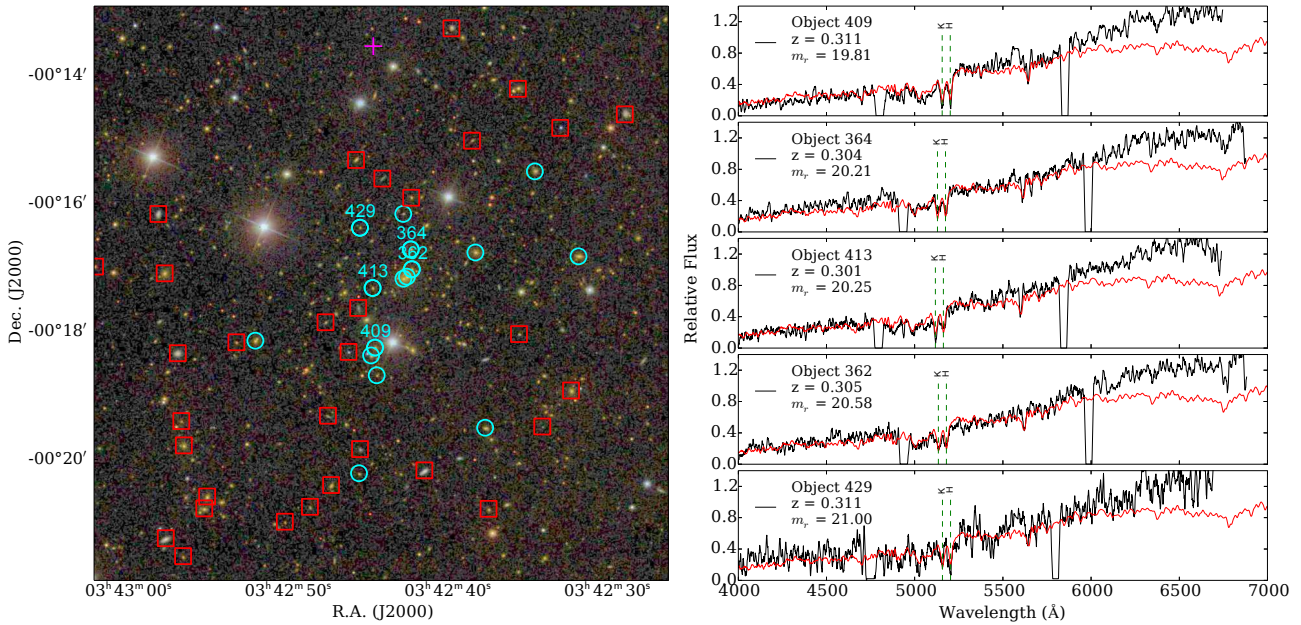
**Table A3.** Spectroscopic redshifts of galaxies in the direction of ACT-CL J0219.9+0129 measured using SALT RSS; see Table 2 for an explanation of the table columns.

ID	Mask	RA (J2000)	Dec. (J2000)	$m_r$	$z$	$Q$	Em. Lines?	Member?	$r$ (Mpc)
370	1	02 <sup>h</sup> 19 <sup>m</sup> 52 <sup>s</sup> .155	+01°29′52″.19	17.96	0.3646	4	...	✓	0.00
397	1	02 <sup>h</sup> 19 <sup>m</sup> 52 <sup>s</sup> .975	+01°29′35″.03	21.29	0.3639	4	...	✓	0.11
410	1	02 <sup>h</sup> 19 <sup>m</sup> 53 <sup>s</sup> .386	+01°30′31″.71	21.22	0.3679	4	...	✓	0.22
434	1	02 <sup>h</sup> 19 <sup>m</sup> 54 <sup>s</sup> .222	+01°29′20″.51	21.01	0.3641	4	...	✓	0.22
390	1	02 <sup>h</sup> 19 <sup>m</sup> 52 <sup>s</sup> .668	+01°29′06″.20	21.01	0.3585	4	...	✓	0.23
1	S	02 <sup>h</sup> 19 <sup>m</sup> 57 <sup>s</sup> .414	+01°30′02″.31	19.45	0.3697	4	...	✓	0.40
4	S	02 <sup>h</sup> 19 <sup>m</sup> 56 <sup>s</sup> .219	+01°30′58″.53	18.56	0.3675	4	...	✓	0.45
395	1	02 <sup>h</sup> 19 <sup>m</sup> 52 <sup>s</sup> .931	+01°31′22″.76	20.08	0.3544	4	...	✓	0.45
379	1	02 <sup>h</sup> 19 <sup>m</sup> 52 <sup>s</sup> .348	+01°28′17″.92	20.17	0.3496	4	...	...	...
508	1	02 <sup>h</sup> 19 <sup>m</sup> 55 <sup>s</sup> .973	+01°31′07″.71	21.23	0.3649	4	...	✓	0.47
309	1	02 <sup>h</sup> 19 <sup>m</sup> 49 <sup>s</sup> .797	+01°31′35″.97	20.67	0.3489	4	...	...	...
407	1	02 <sup>h</sup> 19 <sup>m</sup> 53 <sup>s</sup> .365	+01°31′48″.61	19.11	0.2389	4	...	...	...
447	1	02 <sup>h</sup> 19 <sup>m</sup> 54 <sup>s</sup> .580	+01°27′59″.68	20.91	0.3686	4	...	✓	0.59
274	1	02 <sup>h</sup> 19 <sup>m</sup> 48 <sup>s</sup> .609	+01°27′46″.90	18.53	0.3666	4	...	✓	0.67
428	1	02 <sup>h</sup> 19 <sup>m</sup> 53 <sup>s</sup> .908	+01°32′35″.19	21.45	0.5602	4	...	...	...
5	S	02 <sup>h</sup> 20 <sup>m</sup> 01 <sup>s</sup> .648	+01°28′27″.15	19.19	0.3629	4	...	✓	0.82
450	1	02 <sup>h</sup> 19 <sup>m</sup> 54 <sup>s</sup> .615	+01°26′53″.96	20.06	0.3697	4	...	✓	0.90
229	1	02 <sup>h</sup> 19 <sup>m</sup> 46 <sup>s</sup> .790	+01°26′39″.57	21.61	0.7861	4	✓	...	...
299	1	02 <sup>h</sup> 19 <sup>m</sup> 49 <sup>s</sup> .495	+01°26′20″.61	20.68	0.5314	4	✓	...	...
663	1	02 <sup>h</sup> 20 <sup>m</sup> 02 <sup>s</sup> .912	+01°27′08″.25	21.69	0.3580	3	...	...	...

**Figure A3.** The  $z = 0.36$  cluster ACT-CL J0219.9+0129 (see Fig. 1 for an explanation of symbols and colours).

**Table A4.** Spectroscopic redshifts of galaxies in the direction of ACT-CL J0342.7-0017 measured using SALT RSS; see Table 2 for an explanation of the table columns.

ID	Mask	RA (J2000)	Dec. (J2000)	$m_r$	$z$	$Q$	Em. Lines?	Member?	$r$ (Mpc)
7	S	03 <sup>h</sup> 42 <sup>m</sup> 42 <sup>s</sup> .651	−00°17′08″.29	17.70	0.3072	4	...	✓	0.00
2	S	03 <sup>h</sup> 42 <sup>m</sup> 42 <sup>s</sup> .873	−00°17′10″.22	18.20	0.3127	4	...	✓	0.02
362	1	03 <sup>h</sup> 42 <sup>m</sup> 42 <sup>s</sup> .346	−00°17′01″.28	20.58	0.3052	4	...	✓	0.04
364	1	03 <sup>h</sup> 42 <sup>m</sup> 42 <sup>s</sup> .414	−00°16′42″.67	20.21	0.3039	4	...	✓	0.11
413	1	03 <sup>h</sup> 42 <sup>m</sup> 44 <sup>s</sup> .804	−00°17′18″.92	20.25	0.3009	4	...	✓	0.15
432	1	03 <sup>h</sup> 42 <sup>m</sup> 45 <sup>s</sup> .707	−00°17′37″.69	20.47	0.1658	3	...	...	...
374	1	03 <sup>h</sup> 42 <sup>m</sup> 42 <sup>s</sup> .883	−00°16′09″.36	20.86	0.3010	4	✓	✓	0.26
429	1	03 <sup>h</sup> 42 <sup>m</sup> 45 <sup>s</sup> .595	−00°16′22″.35	21.00	0.3111	4	...	✓	0.29
8	S	03 <sup>h</sup> 42 <sup>m</sup> 38 <sup>s</sup> .364	−00°16′45″.57	18.67	0.3111	4	...	✓	0.30
409	1	03 <sup>h</sup> 42 <sup>m</sup> 44 <sup>s</sup> .651	−00°18′14″.94	19.81	0.3107	4	...	✓	0.33
363	1	03 <sup>h</sup> 42 <sup>m</sup> 42 <sup>s</sup> .387	−00°15′54″.14	20.23	0.7064	4	...	...	...
25	S	03 <sup>h</sup> 42 <sup>m</sup> 44 <sup>s</sup> .899	−00°18′22″.30	19.86	0.3129	4	...	✓	0.36
474	1	03 <sup>h</sup> 42 <sup>m</sup> 47 <sup>s</sup> .751	−00°17′51″.14	20.56	0.1654	4	...	...	...
400	1	03 <sup>h</sup> 42 <sup>m</sup> 44 <sup>s</sup> .194	−00°15′36″.13	20.57	0.2384	4	✓	...	...
407	1	03 <sup>h</sup> 42 <sup>m</sup> 44 <sup>s</sup> .546	−00°18′40″.94	20.95	0.3019	4	...	✓	0.43
216	1	03 <sup>h</sup> 42 <sup>m</sup> 35 <sup>s</sup> .633	−00°18′02″.22	20.77	0.3664	4	✓	...	...
436	1	03 <sup>h</sup> 42 <sup>m</sup> 45 <sup>s</sup> .840	−00°15′18″.69	19.50	0.2393	4	...	...	...
274	1	03 <sup>h</sup> 42 <sup>m</sup> 38 <sup>s</sup> .579	−00°15′00″.56	20.70	0.0191	3	...	...	...
473	1	03 <sup>h</sup> 42 <sup>m</sup> 47 <sup>s</sup> .601	−00°19′18″.95	20.62	0.2863	4	✓	...	...
26	S	03 <sup>h</sup> 42 <sup>m</sup> 34 <sup>s</sup> .639	−00°15′29″.36	18.95	0.3043	4	...	✓	0.69
42	S	03 <sup>h</sup> 42 <sup>m</sup> 52 <sup>s</sup> .148	−00°18′08″.46	18.98	0.3042	4	...	✓	0.69
260	1	03 <sup>h</sup> 42 <sup>m</sup> 37 <sup>s</sup> .754	−00°19′30″.24	19.15	0.3033	4	...	✓	0.71
5	S	03 <sup>h</sup> 42 <sup>m</sup> 31 <sup>s</sup> .905	−00°16′49″.20	18.74	0.3113	4	...	✓	0.72
428	1	03 <sup>h</sup> 42 <sup>m</sup> 45 <sup>s</sup> .590	−00°19′50″.29	20.61	0.1116	4	✓	...	...
430	1	03 <sup>h</sup> 42 <sup>m</sup> 45 <sup>s</sup> .654	−00°20′12″.98	20.77	0.3093	4	...	✓	0.85
468	1	03 <sup>h</sup> 42 <sup>m</sup> 47 <sup>s</sup> .405	−00°20′24″.07	19.67	0.3656	4	...	...	...
498	1	03 <sup>h</sup> 42 <sup>m</sup> 48 <sup>s</sup> .728	−00°20′44″.52	20.80	0.2869	4	✓	...	...
521	1	03 <sup>h</sup> 42 <sup>m</sup> 50 <sup>s</sup> .300	−00°20′58″.49	21.30	0.4619	4	...	...	...

**Figure A4.** The  $z = 0.30$  cluster ACT-CL J0342.7-0017 (see Fig. 1 for an explanation of symbols and colours).



**Table A5.** Spectroscopic redshifts of galaxies in the direction of ACT-CL J0348.6-0028 measured using SALT RSS; see Table 2 for an explanation of the table columns.

ID	Mask	RA (J2000)	Dec. (J2000)	$m_r$	$z$	$Q$	Em. Lines?	Member?	$r$ (Mpc)
274	3	03 <sup>h</sup> 48 <sup>m</sup> 39 <sup>s</sup> .545	−00°28′16″90	19.22	0.3450	4	...	✓	0.00
252	4	03 <sup>h</sup> 48 <sup>m</sup> 38 <sup>s</sup> .726	−00°28′07″42	18.13	0.1381	4	...	...	...
246	1	03 <sup>h</sup> 48 <sup>m</sup> 38 <sup>s</sup> .378	−00°28′23″21	20.49	0.3443	4	...	✓	0.09
229	4	03 <sup>h</sup> 48 <sup>m</sup> 37 <sup>s</sup> .682	−00°28′20″77	20.07	0.1393	4	...	...	...
303	1	03 <sup>h</sup> 48 <sup>m</sup> 41 <sup>s</sup> .534	−00°28′07″50	19.87	0.3443	4	...	✓	0.16
230	1	03 <sup>h</sup> 48 <sup>m</sup> 37 <sup>s</sup> .699	−00°28′36″14	20.40	0.3416	4	...	✓	0.16
232	3	03 <sup>h</sup> 48 <sup>m</sup> 37 <sup>s</sup> .909	−00°28′46″75	21.04	0.3448	3	...	✓	0.19
315	3	03 <sup>h</sup> 48 <sup>m</sup> 42 <sup>s</sup> .291	−00°28′29″17	21.08	0.3490	3	...	✓	0.22
218	2	03 <sup>h</sup> 48 <sup>m</sup> 37 <sup>s</sup> .125	−00°27′48″38	18.17	0.1603	4	...	...	...
264	1	03 <sup>h</sup> 48 <sup>m</sup> 39 <sup>s</sup> .134	−00°29′05″30	21.02	0.3503	4	...	✓	0.24
312	1	03 <sup>h</sup> 48 <sup>m</sup> 42 <sup>s</sup> .151	−00°28′48″76	19.76	0.3462	4	...	✓	0.25
304	2	03 <sup>h</sup> 48 <sup>m</sup> 41 <sup>s</sup> .593	−00°27′35″15	19.48	0.5471	4	...	...	...
207	1	03 <sup>h</sup> 48 <sup>m</sup> 36 <sup>s</sup> .300	−00°27′49″82	20.50	0.3401	4	...	✓	0.27
308	3	03 <sup>h</sup> 48 <sup>m</sup> 42 <sup>s</sup> .024	−00°28′58″10	21.09	0.3420	4	...	✓	0.28
239	1	03 <sup>h</sup> 48 <sup>m</sup> 38 <sup>s</sup> .081	−00°29′18″25	20.68	0.3482	4	...	✓	0.32
330	3	03 <sup>h</sup> 48 <sup>m</sup> 43 <sup>s</sup> .143	−00°27′31″36	20.92	0.3450	4	...	✓	0.35
215	1	03 <sup>h</sup> 48 <sup>m</sup> 36 <sup>s</sup> .792	−00°27′12″79	20.54	0.3505	4	...	✓	0.38
255	4	03 <sup>h</sup> 48 <sup>m</sup> 38 <sup>s</sup> .949	−00°26′50″01	21.29	0.3443	4	...	✓	0.43
181	4	03 <sup>h</sup> 48 <sup>m</sup> 34 <sup>s</sup> .662	−00°29′07″57	21.34	0.3570	4	...	...	...
165	3	03 <sup>h</sup> 48 <sup>m</sup> 33 <sup>s</sup> .621	−00°28′04″90	20.68	0.3446	4	...	✓	0.44
358	3	03 <sup>h</sup> 48 <sup>m</sup> 45 <sup>s</sup> .127	−00°27′45″73	20.81	0.2938	4	✓	...	...
272	2	03 <sup>h</sup> 48 <sup>m</sup> 39 <sup>s</sup> .430	−00°26′39″99	20.69	0.1803	3	✓	...	...
237	1	03 <sup>h</sup> 48 <sup>m</sup> 37 <sup>s</sup> .972	−00°26′40″69	20.56	0.3459	4	...	✓	0.49
153	2	03 <sup>h</sup> 48 <sup>m</sup> 32 <sup>s</sup> .984	−00°27′17″87	22.25	0.4894	3	...	...	...
206	1	03 <sup>h</sup> 48 <sup>m</sup> 36 <sup>s</sup> .276	−00°30′01″29	20.94	0.3456	4	...	✓	0.57
169	3	03 <sup>h</sup> 48 <sup>m</sup> 33 <sup>s</sup> .978	−00°30′01″20	20.46	0.2963	4	...	...	...
320	1	03 <sup>h</sup> 48 <sup>m</sup> 42 <sup>s</sup> .708	−00°25′44″78	20.20	0.3602	3	...	...	...
371	3	03 <sup>h</sup> 48 <sup>m</sup> 45 <sup>s</sup> .867	−00°30′25″66	21.75	0.3342	4	...	...	...
149	4	03 <sup>h</sup> 48 <sup>m</sup> 32 <sup>s</sup> .871	−00°30′22″95	21.29	0.3400	4	...	✓	0.79
270	4	03 <sup>h</sup> 48 <sup>m</sup> 39 <sup>s</sup> .412	−00°25′30″78	19.13	0.3516	4	...	✓	0.82
98	3	03 <sup>h</sup> 48 <sup>m</sup> 28 <sup>s</sup> .95	−00°29′10″64	20.20	0.3412	4	...	✓	0.83
107	3	03 <sup>h</sup> 48 <sup>m</sup> 29 <sup>s</sup> .523	−00°29′31″57	20.86	0.3084	4	...	...	...
231	1	03 <sup>h</sup> 48 <sup>m</sup> 37 <sup>s</sup> .854	−00°25′21″24	20.67	0.3515	4	...	✓	0.88
258	1	03 <sup>h</sup> 48 <sup>m</sup> 39 <sup>s</sup> .012	−00°31′35″60	20.27	0.3891	4	...	...	...
401	1	03 <sup>h</sup> 48 <sup>m</sup> 48 <sup>s</sup> .183	−00°31′03″08	20.82	0.4575	4	...	...	...
141	1	03 <sup>h</sup> 48 <sup>m</sup> 32 <sup>s</sup> .555	−00°31′24″45	19.99	0.2950	4	...	...	...
136	1	03 <sup>h</sup> 48 <sup>m</sup> 32 <sup>s</sup> .246	−00°25′03″39	20.76	0.3412	3	...	...	...
174	2	03 <sup>h</sup> 48 <sup>m</sup> 34 <sup>s</sup> .196	−00°31′48″88	21.63	0.4168	3	✓	...	...
99	3	03 <sup>h</sup> 48 <sup>m</sup> 29 <sup>s</sup> .063	−00°25′15″83	20.34	0.3422	3	...	...	...

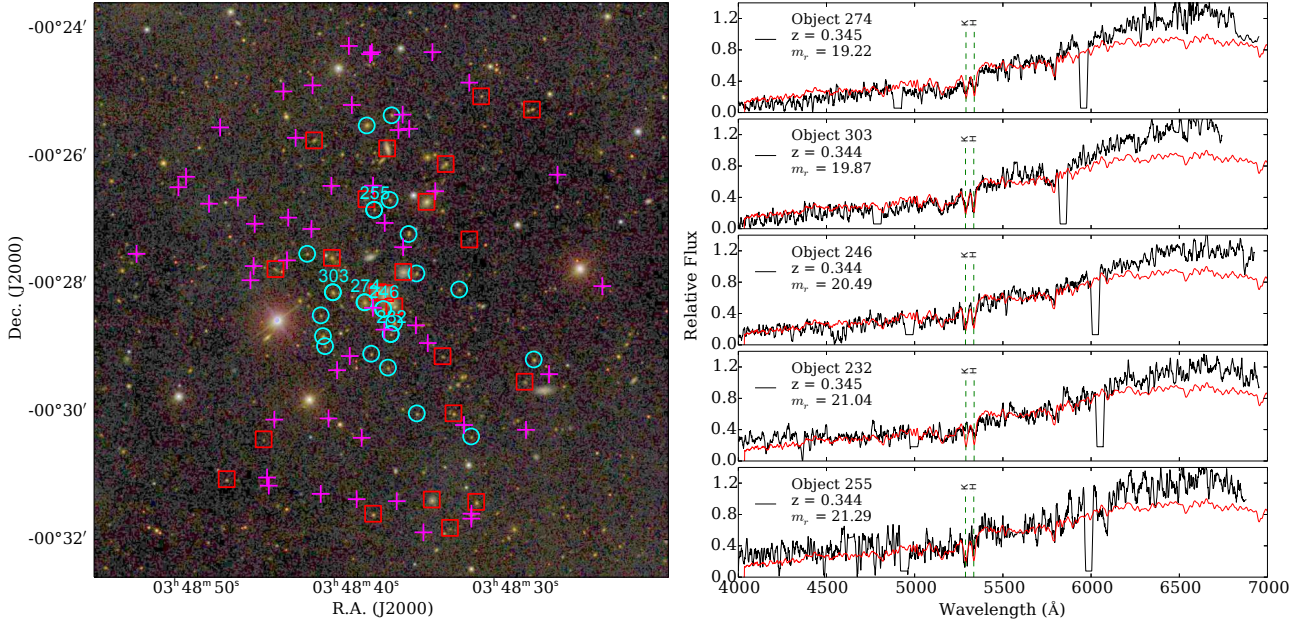


**Figure A5.** The  $z = 0.35$  cluster ACT-CL J0348.6-0028 (see Fig. 1 for an explanation of symbols and colours).

**Table A6.** Spectroscopic redshifts of galaxies in the direction of ACT-CL J2058.8+0123 measured using SALT RSS; see Table 2 for an explanation of the table columns.

ID	Mask	RA (J2000)	Dec. (J2000)	$m_r$	$z$	$Q$	Em. Lines?	Member?	$r$ (Mpc)
219	2	20 <sup>h</sup> 58 <sup>m</sup> 56 <sup>s</sup> .777	+01°22′47″.58	19.66	0.3383	4	...	...	...
225	3	20 <sup>h</sup> 58 <sup>m</sup> 57 <sup>s</sup> .187	+01°21′51″.00	19.72	0.3207	4	...	✓	0.16
194	1	20 <sup>h</sup> 58 <sup>m</sup> 54 <sup>s</sup> .089	+01°22′24″.07	20.71	0.3227	3	...	✓	0.27
173	2	20 <sup>h</sup> 58 <sup>m</sup> 52 <sup>s</sup> .683	+01°22′14″.21	19.86	0.2043	4	...	...	...
211	1	20 <sup>h</sup> 58 <sup>m</sup> 55 <sup>s</sup> .861	+01°21′03″.94	20.73	0.3270	3	...	✓	0.39
201	2	20 <sup>h</sup> 58 <sup>m</sup> 54 <sup>s</sup> .572	+01°20′59″.56	20.54	0.3293	4	...	✓	0.45
184	1	20 <sup>h</sup> 58 <sup>m</sup> 53 <sup>s</sup> .730	+01°23′36″.04	20.83	0.3148	4	...	...	...
164	2	20 <sup>h</sup> 58 <sup>m</sup> 52 <sup>s</sup> .060	+01°21′40″.62	19.50	0.3334	4	...	✓	0.46
213	1	20 <sup>h</sup> 58 <sup>m</sup> 56 <sup>s</sup> .096	+01°20′41″.27	20.44	0.3286	4	...	...	...
203	2	20 <sup>h</sup> 58 <sup>m</sup> 54 <sup>s</sup> .836	+01°20′35″.18	18.00	0.3311	4	✓	...	...
177	1	20 <sup>h</sup> 58 <sup>m</sup> 53 <sup>s</sup> .056	+01°24′10″.76	18.13	0.3301	4	...	✓	0.61
157	2	20 <sup>h</sup> 58 <sup>m</sup> 51 <sup>s</sup> .547	+01°23′54″.82	21.00	0.3260	4	...	✓	0.62
200	1	20 <sup>h</sup> 58 <sup>m</sup> 54 <sup>s</sup> .514	+01°24′26″.77	20.55	0.3317	4	...	✓	0.63
137	3	20 <sup>h</sup> 58 <sup>m</sup> 50 <sup>s</sup> .390	+01°23′56″.26	19.60	0.3265	4	...	✓	0.69
166	2	20 <sup>h</sup> 58 <sup>m</sup> 52 <sup>s</sup> .163	+01°24′30″.79	20.38	0.3239	4	...	✓	0.72
162	2	20 <sup>h</sup> 58 <sup>m</sup> 51 <sup>s</sup> .745	+01°24′45″.88	20.97	0.3281	4	...	✓	0.80
190	1	20 <sup>h</sup> 58 <sup>m</sup> 53 <sup>s</sup> .906	+01°25′24″.84	19.60	0.1856	4	✓	...	...
146	2	20 <sup>h</sup> 58 <sup>m</sup> 50 <sup>s</sup> .917	+01°25′22″.66	19.69	0.3228	4	✓	✓	0.98
150	1	20 <sup>h</sup> 58 <sup>m</sup> 51 <sup>s</sup> .379	+01°19′14″.61	19.92	0.3222	4	✓	...	...
90	3	20 <sup>h</sup> 58 <sup>m</sup> 46 <sup>s</sup> .076	+01°24′52″.59	18.14	0.2935	4	✓	...	...
153	1	20 <sup>h</sup> 58 <sup>m</sup> 51 <sup>s</sup> .408	+01°25′57″.05	19.66	0.3321	4	...	✓	1.10
210	2	20 <sup>h</sup> 58 <sup>m</sup> 55 <sup>s</sup> .832	+01°26′29″.51	20.27	0.1346	4	...	...	...
136	1	20 <sup>h</sup> 58 <sup>m</sup> 50 <sup>s</sup> .317	+01°26′09″.59	21.34	0.3249	4	✓	✓	1.19
165	3	20 <sup>h</sup> 58 <sup>m</sup> 52 <sup>s</sup> .163	+01°26′23″.63	17.86	0.1344	4	...	...	...

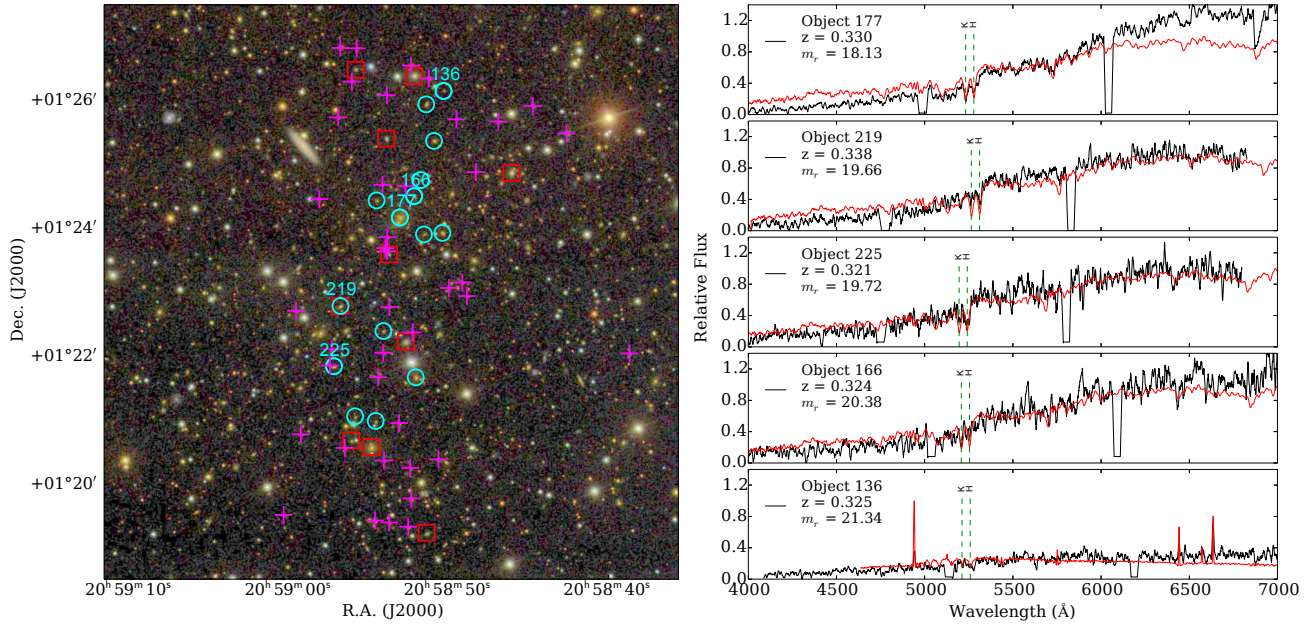


**Figure A6.** The  $z = 0.33$  cluster ACT-CL J2058.8+0123 (see Fig. 1 for an explanation of symbols and colours).